CENTRO DE INVESTIGACIONES
EN OPTICA, A.C.

“STUDIES OF HYDRODYNAMIC WITH T-DHI AND BONE MECHANICAL INTEGRITY USING DHI AND FD-OCT”

To obtain the Doctor of Science (Optics) Degree

Presented by: MS. Brenda Mireya Guzmán Valdivia

Advisor: Dr. Manuel Humberto De La Torre Ibarra

Aguascalientes Aguascalientes · México

Agosto de 2024

Dedicatory

To my parents.

Mom, I feel your blessing from Heaven.

Dad, thank you for always be by my side.

I love you.

Acknowledgments

It has been a long journey since I decided to begin a PhD. I have experienced and learned so much about the doctorate, but I have also learned about life: we live, and we die, as simple as that, and in the end, what really matters are the moments we share with others.

I am grateful to God for letting me share my path with wonderful people who accompanied me throughout the entire process. First, I want to thank my parents for always being by my side, offering their unwavering love and support. If I have come this far, it is because of them. I also thank my brother for always having the right words to encourage me.

From the bottom of my heart, I thank my husband, Edgar, for being a source of love, understanding, and tenderness throughout this journey. You gave me the strength to overcome every challenge along the way. I'm grateful to share the best stories with you.

I also want to express my appreciation and gratitude to my adviser, Dr. Manuel De La Torre, for his guidance, mentorship, and expertise, which contributed significantly to my academic and personal growth. His words and advise provided comfort during the difficulties I experienced throughout the doctorate.

I want to thank the evaluation committee, Dra. Maria del Socorro Hernández, Dr. Mauricio Flores Moreno, and Dr. Claudio Frausto Reyes, for your time revising the progress of this project. I also thank Dr. Fernando Mendoza Santoyo for accepting being part of the synod.

To my lab-mates, Gloria, Ángel, and Javier, for their advice and support.

Finally, I want to thank CONAHCYT for the financial support I received during my studies.

Contents

Figure list

Table list

Abstract

Optical metrology encompasses many methods that use light to analyze and quantify the properties of diverse materials and their applications. Interferometric-based techniques are part of these methods and offer non-invasive, remote measurement capabilities with a high-resolution material inspection. They are categorized as superficial or internal inspections from opaque objects and in transmission for transparent media.

The first study involves the transmission Digital Holographic Interferometry (t-DHI) method to measure fluid dynamics inside a scale water tunnel designed as a simile of a wind tunnel. The water tunnel has a transparent chamber where the optical system observes the hydrodynamics from the water and a sample. As proof of principle, three tests are presented to validate the similarity of the system with an aerodynamic test. For this purpose, a scale model car magnetically placed inside the chamber is tested to detect its drag due to a laminar flow moving in the tunnel. The results prove that t-DHI has the potential to be used as an alternative to traditional wind tunnels.

In the second study, a dual configuration using Digital Holographic Interferometry (DHI) and Fourier Domain Optical Coherence Tomography (FD-OCT) simultaneously explores the mechanical change of mice femoral bones stored in different solutions. The influence of the storage media on the viscoelastic properties of the tissue is analyzed by employing a three-point bending test. Three bone groups are prepared, a control with fresh post-mortem samples. The second and third groups use saline and formaldehyde solutions as storage media. The high sensitivity of the optical techniques makes it possible to observe changes in the anisotropy of the samples. As a comparison, Raman spectroscopy analyses the three bone groups to prove that the preservation media does not affect a single-point inspection as the full-field one.

1. Introduction

Optical metrology is measuring using light to analyze and quantify the physical properties of diverse objects and materials [1]. The measurements could include distance, shape, displacement, stress, and speed [2-6]. Its application ranges from manufacturing and engineering to biology and medicine. Several methods and techniques are devoted to these purposes. Among them are the interferometry-based methods, known for their high sensitivity and proven efficacy in many scientific and industrial fields. An interferometric group of these methods uses the reconstruction of a wavefront distorted by an object under study.

Techniques based on this principle include using two or more light beams to retrieve an interference pattern. The latter can be used to have a measurement from the object indirectly. Since light is used as the measuring tool, the resolution is on the scale of the wavelength of the illumination source, generally in fractions of microns. A resolution that is hard to achieve with conventional mechanical instruments. A distinctive advantage of the interferometric techniques lies in their non-invasive, non-contact, and remote measurement capabilities [7-10]. The possible materials that can be analyzed include composites, biological tissues, transparent media, and engineering materials [11-14]. The type of inspection for these materials can be categorized as superficial, internal, or in transmission, depending on the material, measurement, and technique employed.

Digital Holographic Interferometry (DHI) and Fourier Domain Optical Coherence Tomography (FD-OCT) are examples of interferometric techniques that perform superficial and internal inspections, respectively. Both techniques retrieve full-field information from opaque and low-scattered materials [15,16]. Even more, DHI in a modified configuration (transmission mode, t-DHI) enables the examination of transparent materials [17]. These techniques retrieve optical phase differences between two different conditions of an object under study, which helps study dynamic and non-repeatable events.

The present document explores the potential of interferometric techniques (DHI and FD-OCT) to analyze different aspects of materials in transmission, surface, and inner inspections. For this purpose, two distinct yet related research studies are proposed.

The first one performs a novel study in transparent media, where fluid interactions within a water tunnel are observed. Here, not only is the capability of t-DHI for capturing real-time, high-resolution data in transparent media shown, but it also has the potential to retrieve full-field fluid dynamic information similar to an aerodynamic study. Experimental tests commonly use wind tunnels or water channels to study fluid dynamics. The use and implementation of these robust systems are expensive and require specific hardware and skilled personnel for each test; typically, in huge spaces, viz., a small wind tunnel's length could range from 6 to 9 meters [18,19]. Also, a circulating water channel for open water tests could have sections of several meters [20]. When a test is performed, a common practice is to attach sensors to the object under study to obtain parameters like pressure, velocity, and drift or drag coefficient. However, this practice has some limitations, as only those points where the sensors are situated retrieve information [21-23]. Additional agents are sometimes added to the tunnel, like smoke pipelines for flow visualization [24] or particles to be tracked [25].

Numerical simulation is an alternative to reduce the experimental costs due to the continuous use of these specialized facilities. Here, the objective is to predict the flow's interaction with different objects [26-30]. Nevertheless, even when the computer analysis has proved helpful, it usually assumes ideal conditions for the simulation, as the real environmental conditions are complex variables to be introduced. For this reason, some results are approximated or biased. The accurate and real full-field study of dynamic interactions calls for new methodologies that need to be explored, for instance, optical non-destructive methods, to analyze transparent media such as flows [30]; however, a large-scale test is challenging to carry out with interferometric techniques/methods. Nevertheless, a down-scaled measurement could faithfully reproduce the response of a sample of interest.

DHI is a non-destructive optical method [31,32] that can be modified to detect phase changes in transmission mode, t-DHI [33]. The system's sensitivity is improved by using a collimated beam in the object's arm of the interferometer. This characteristic allows the detection of disturbances in large transparent media sections [34]. This work applies this t-DHI to a water tunnel where a slow laminar flow is introduced to interact with different samples. The water tunnel has a rectangular and transparent section (called the chamber) where the t-DHI interferometer's object beam interacts with the liquid to analyze the presence-occurrence of disturbances.

The hydrodynamic information retrieved with the t-DHI system is tested with different objects inside the water tunnel once at a time. The first test analyses the water tunnel's flow movement with no object inside the chamber. This experiment aims to verify that the water introduced in the chamber shows a laminar flow. Here, the flow direction is produced by the water when it enters the chamber in a controlled form. A well-known geometry is used for a second test: a square plaque blocking half of the water's path inside the chamber is placed to induce a flow change trajectory. The last test uses a scale model car magnetically placed inside the chamber to register its interaction with the laminar flow in the tunnel. The retrieved optical phase from all tests makes it possible to observe a hydrodynamic behavior comparable with those reported in the literature for simulations and experiments where the air is used (wind tunnel). The similarity between these two methods is possible in this scale water tunnel as the optical phase sensitivity requires micro water displacements to retrieve a displacement measurement. The proposed configuration in this work could be used as an alternative to aerodynamic tests in wind tunnels with the advantage of having simpler and small-size hardware and, maybe, also important, a cost-reduced facility.

The second research employs a dual configuration of a DHI combined with an FD-OCT setup [35], applied to study the mechanical behavior of bones stored in different solutions. The integration of both techniques enables the analysis of surface and internal inspections simultaneously while offering insights into the properties of opaque and low-scattered biological materials. The bone is a calcified structure composed of 60% inorganic component (hydroxyapatite), 30% organic component (proteins and collagen), and 10% of water [36]. The bone's anisotropy and viscoelasticity maximize its strength relative to mechanical stimuli, and at the same time, they give it lightness [37]. Mechanical properties of the bone, such as stress, fatigue, or stiffness, have been measured with different techniques [38-41]. As human bone is restricted and controlled, most of the reported research uses mice, porcine, or bovine bones for their studies under specific considerations [42-45]. In particular, ex-vivo samples must be tested immediately after the sample is retrieved. However, as this

condition is not always possible, the tissue must be immersed in a preservation media for posterior analysis. Saline and formaldehyde solutions are the most common and applied solutions to preserve hard tissues like bones [46,47]. Nevertheless, since the analysis of bones generally deals with their chemical properties to determine their composition [48], the preservation solution has no significant consideration over the anisotropy of the mechanical response, as this is not subsequently tested. However, determining which preservation method affects the bone's mechanical properties less is relevant because new medical investigations use the bone's response to measure their impact [49,50].

Mice femoral bones are used to analyze the impact of the preservation media in their whole mechanical response since mice are typically used in investigation as a first stage before testing over other organisms. As mentioned, DHI and FD-OCT are used simultaneously to analyze the mechanical response of mice femoral bones preserved in different media under a well-known mechanical test [51]. Both techniques can retrieve a biological material's mechanical response as a displacement map [52-54]. For DHI, the obtained response comes from the sample's surface [55-57], while for FD-OCT, it comes from the inner layers. Each mouse femoral bone is mechanically deformed using a standard three-point bending (3PB) test [58]. Three groups of femurs are set; one is a fresh post-mortem group (PM), which works as the control group. A second group is preserved in saline solution (SS), and a third group is preserved in formaldehyde solution (FM). The last two groups remain for 48 hours in the preservation solution before they are tested. By comparing the applied displacement information of the fresh and stored groups, it is possible to observe that the FM solution affects the anisotropy of the bones while the SS keeps the viscoelastic response similar to the fresh bone group. Internal measurements also indicate marrow damage when FM solution is used, even in this short time. The latter could be detected and measured thanks to the high surface and internal optical phase sensitivity.

By linking these projects, this thesis shows the versatility of interferometric techniques in capturing dynamic events and highlights their potential for new applications over complex phenomena. This work presents novel applications of interferometry in opaque surfaces (backscattering), transparent media (transmission), and under the surface (internal).

2. Theory

This chapter introduces the basic theoretical concepts required for the work: fluid analysis, bone structure, and speckle pattern interferometry, among others. It is presented in four main sections; the first is devoted to the DHI method and how it is used to measure surface deformations in opaque samples in an out-of-plane configuration. Besides, it introduces the analysis of transparent media with a transmission mode configuration. The second section deals with the FD-OCT technique beyond the tomographic image. It describes how the displacement information is retrieved within a low-scattering medium such as a bone. The third section describes fluid dynamics with its model for the hydrodynamic device introduced in this work. Finally, the fourth section comprehensively describes the bone tissue from a mechanical point of view.

2.1. Basic Concepts of Digital Holographic Interferometry

2.1.1 Holography

Holography is a well-known method used to record and reconstruct optical wave fields. Dennis Gabor invented it at the end of the forties for electron microscopy [59]. Later, in the 1960s, with the development of lasers, the applicability of Holography was extended. Its principle is to record the wavefront information from an object by registering its interference pattern with a reference wave; this pattern is called a hologram. Then, the wavefront object is reconstructed by illuminating the developed hologram with a replica of the reference beam used during the initial recording. With this reconstructed wavefront, an observer will see a virtual three-dimensional image of the original object.

Holograms were recorded on a photographic plate, which generated a three-dimensional image of the object. For conventional image recording, like photographs, the original scene is recorded only through its intensity distribution, which results in the loss of optical path information, so it is impossible to recover the phase. Holography is characterized by recording both the optical phase and the amplitude of the waves coming from the object. However, since all the recording materials are only sensitive to the intensity signal, it is necessary to record intensity variations related to a reference beam to retrieve the phase. The latter means that a coherent illumination source is split into a beam to illuminate the object, while the second beam is used as a reference beam [60].

2.1.2 Recording and reconstruction of a hologram

A typical configuration for hologram recording is shown in Figure 1. Here, the coherent illumination source is divided by a beam splitter (BS) into the object (OB) and reference (RB) beams, which are directed by mirrors M1-M4. The first one is directed with a mirror to illuminate the object's surface, where its backscattering is recorded over the holographic media. The reference beam illuminates the recording media directly. Both beams

interfere with each other over the media, and the recorded interference pattern is the hologram.

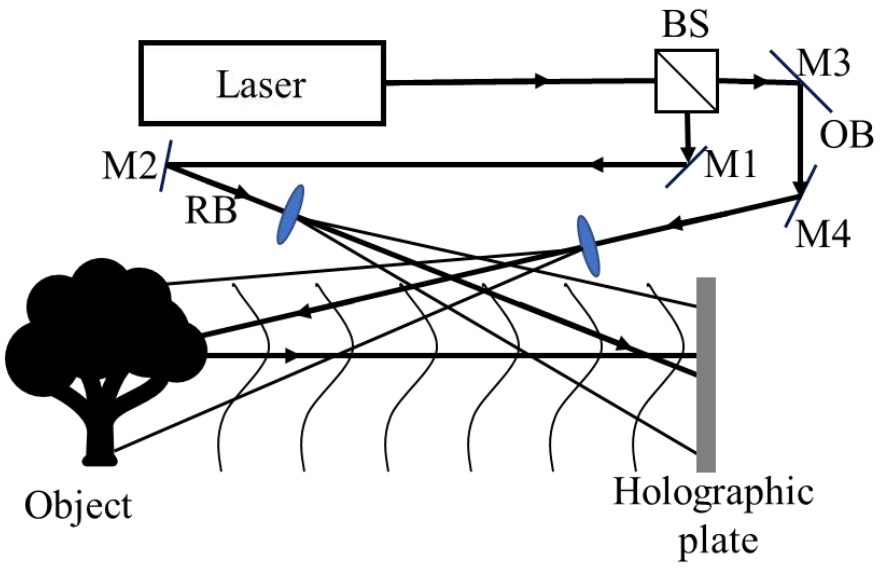

Figure 1. Typical hologram recording configuration.

The following expressions describe the amplitude of the object and reference beams:

$$O(x,y) = o(x,y)\exp\{i\varphi_o(x,y)\}, \quad (2.1)$$

$$R(x,y) = r(x,y)\exp\{i\varphi_r(x,y)\}, \quad (2.2)$$

where $o(x,y)$ and $r(x,y)$ are the real part of the amplitude of the object and reference beam, respectively. The terms $\varphi_o(x,y)$, and $\varphi_r(x,y)$ correspond to the optical phase for each beam. The interference signal between both beams over the recording media is described by,

$$\begin{aligned} I(x,y) &= |O(x,y) + R(x,y)|^2 \\ &= (O(x,y) + R(x,y))(O(x,y) + R(x,y))^* \\ &= |O(x,y)|^2 + |R(x,y)|^2 + O(x,y)R^*(x,y) + R(x,y)O^*(x,y). \end{aligned} \quad (2.3)$$

For this expression, it is possible to see that the hologram has the intensity amplitude signal for each beam, $|O(x,y)|^2$ and $|R(x,y)|^2$, with two terms with a conjugate term (*), which are $O(x,y)R^*(x,y)$ and $R(x,y)O^*(x,y)$. These two last terms are associated with the

virtual and the real image. For a recording media like a holographic plate, its amplitude's transmission $h(x, y)$ is proportional to $I(x, y)$,

$$h(x, y) = h_0 \beta \tau I(x, y). \quad (2.4)$$

Constant β is the slope of the amplitude's transmittance vs exposition's characteristics of the material, τ represents the exposition time, and h_0 is the amplitude's transmission from the non-exposed plate. The term $h(x, y)$ is called the hologram expression.

The original object beam can be reconstructed by illuminating the hologram with the reference beam, as shown in Figure 2. A light block (LB) stops the object's beam used during the hologram recording. An observer watches a virtual image of the object that exhibits all of the perspective and depth effects of the original object. [60]

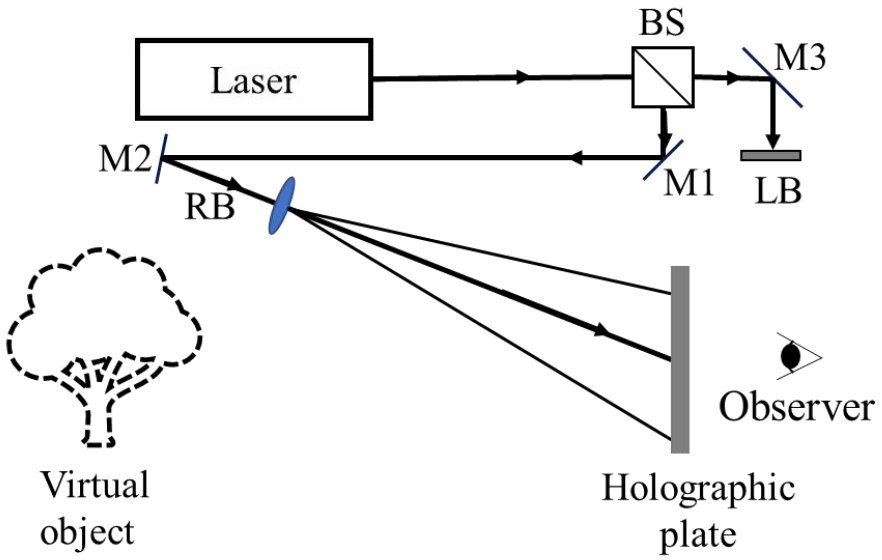

Figure 2. Holographic wavefront reconstruction.

The holographic reconstruction is the modulation result of the reference wave with the transmission term $h(x, y)$.

$$R(x, y)h(x, y)$$
$$= h_0[\beta\tau(r^2 + o^2)R(x, y) + \beta\tau r^2 O(x, y) + \beta\tau R^2(x, y)O^*(x, y)] \,. \quad (2.5)$$

Here, the first term on the right side of the expression represents the non-refracted wave that passes through the hologram. The second term is the reconstructed object beam that forms the virtual image; here $\beta\tau r^2$ only affects the brightness of the image. The last term generates a distorted real image of the object. It is worth mentioning that in off-axis holographic configuration, the virtual and real images and the non-refracted wave are spatially separated.

2.1.3 Holographic interferometry

As mentioned before, holography is a technique that allows the register and reconstruction of wave fields. The precision of this method allows the interferometric comparison of wave fields. Then, holographic interferometry compares two or more wave fields, where at least one is holographically reconstructed. The latter allows the measurement of variations along the optical path length caused by deformation, i.e., an object vibrating. However, only slight differences between the compared wave fields are allowed (within the range of micro deformations). When variations remain within a small range, the change of the wavefield will vary the phase smoothly, forming an interference pattern or holographic interferogram. [61]

2.1.4 Double exposure holographic interferometry

In a double exposure method, two consecutive holograms are recorded for the same object but in two different states. The first represents a reference state, and the second is a modified state, where a physical parameter of the object has been changed. Figure 3 shows, as a schematic, the recording process of both conditions over the same photographic plate. After the recording, the hologram is reconstructed when illuminated with the reference beam (see Figure 4). Here, an overlapped image of interference fringes is visible due to the superposition of both recorded holograms.

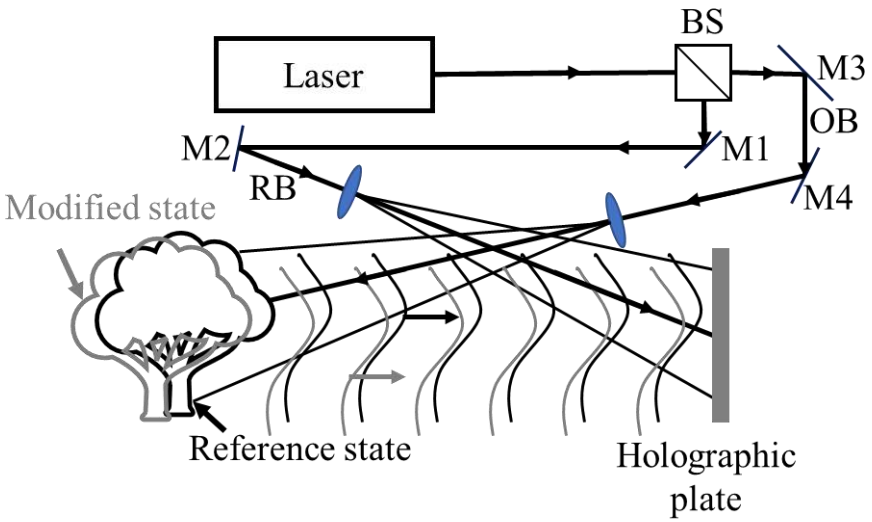

Figure 3. Recording of a double exposure holographic interferogram.

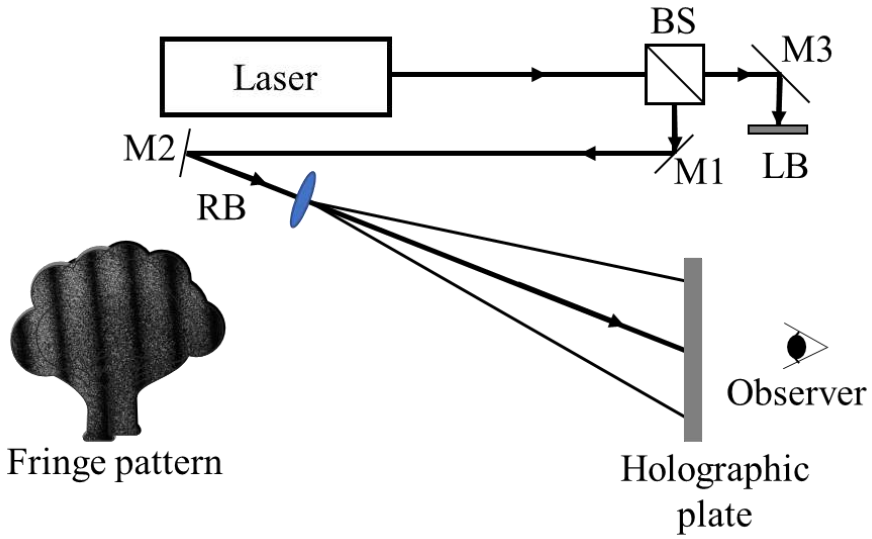

Figure 4. Reconstruction of a double exposure holographic interferogram.

Considering that the complex amplitude from the object's wave at its reference state is holographically recorded, this can be described as follows:

$$E_1(x,y) = a_1(x,y)\exp\{i\phi(x,y)\}, \qquad (2.6)$$

where $a_1(x,y)$ is its real amplitude, and $\phi(x,y)$ is the phase distribution. Then, when a variation over a physical parameter changes the phase distribution from $\phi(x,y)$ to $\phi(x,y)+\Delta\phi(x,y)$, the complex amplitude from the second wavefront corresponding to the modified state of the object's wave is given by,

$$E_2(x,y) = a_2(x,y)\exp\{i[\phi(x,y)+\Delta\phi(x,y)]\}. \tag{2.7}$$

By recording both holograms within the same recording media, both wave fronts are reconstructed simultaneously, and an interferometric pattern is generated with an intensity distribution [61], like,

$$\begin{aligned} I(x,y) &= |E_1(x,y)+E_2(x,y)|^2 = (E_1+E_2)(E_1+E_2)^* \\ &= |E_1|^2 + |E_2|^2 + E_1{E_2}^* + E_2{E_1}^* \\ &= I_1 + I_2 + \sqrt{I_1 I_2}(\exp\{i\Delta\phi\} + \exp\{-i\Delta\phi\}) \\ &= I_1 + I_2 + 2\sqrt{I_1 I_2}\cos\Delta\phi. \end{aligned} \tag{2.8}$$

A general expression for the interference pattern intensity of Eqn. 2.8 is given by

$$I(x,y) = A(x,y) + B(x,y)\cos\Delta\phi, \tag{2.9}$$

where the parameters $A(x,y)$ and $B(x,y)$ depends on the interferogram space coordinates. The phase change $\Delta\phi$ is called the *phase difference* or *interference phase* [62]. Equation 2.9 describes the interaction between the intensity of the interference pattern and its phase interference (which contains information from the physical parameter variation to be measured). The latter could come from a displacement, deformation, refractive index change, or any other modification on the object.

2.1.5 Digital Holographic Interferometry

Holography records and reconstructs wave fronts, while holographic interferometry allows for the comparison of these wave fronts recorded at different times. Digital Holographic Interferometry (DHI) is a two-state technique that allows the analysis of wave fronts and their comparison without physical reconstruction of the object because the image hologram is recorded over a digital device, like a digital camera (CCD or CMOS sensors). The image holograms are stored for posterior quantitative analyses using a computer.

The recording medium (sensor) limits the maximum spatial frequency that can be resolved for the recorded image holograms. Let θ_{max} be the maximum angle between the object and reference beams, and λ the wavelength coming from the illumination source used to record the hologram; thus, the maximum spatial frequency is given by,

$$f_{max} = \frac{2}{\lambda} \sin \frac{\theta_{max}}{2} . \tag{2.10}$$

Considering that the intensity from Equation 2.9 is recorded over a bi-dimensional arrangement or sensor, with $M \times N$ pixels with individual dimensions $\Delta x \times \Delta y$, the discrete intensity registered by the sensor will be described by $I(m\Delta x, n\Delta y)$. Here, m and n are integer numbers; if the pixels have the same size, then $\Delta x = \Delta y$. By the sampling theorem, the maximum spatial frequency that can be registered on the sensor will be:

$$f_{max} = \frac{1}{2\Delta x}. \tag{2.11}$$

By combining equations (2.10) and (2.11), it is obtained.

$$\theta_{max} = 2 \sin^{-1} \frac{\lambda}{4\Delta x} \approx \frac{\lambda}{2\Delta x}, \tag{2.12}$$

here, the approximation is valid for small angles. When a digital sensor records a hologram, the distance between adjacent pixels will determine the maximum angle between the reference and the object beams [63]. An out-of-plane DHI configuration is presented in Figure 5, where the object and reference beams are directed by means of two optical fibers. The optical path difference between the object and the reference arms must be smaller than the coherence length of the illumination source. The out-of-plane refers to the sensitivity direction where the optical system detects changes; in this case, they are perpendicular to its surface. Since DHI is a two-state technique, it requires two image holograms to retrieve the optical phase difference between them (instants before and after the object suffers a change).

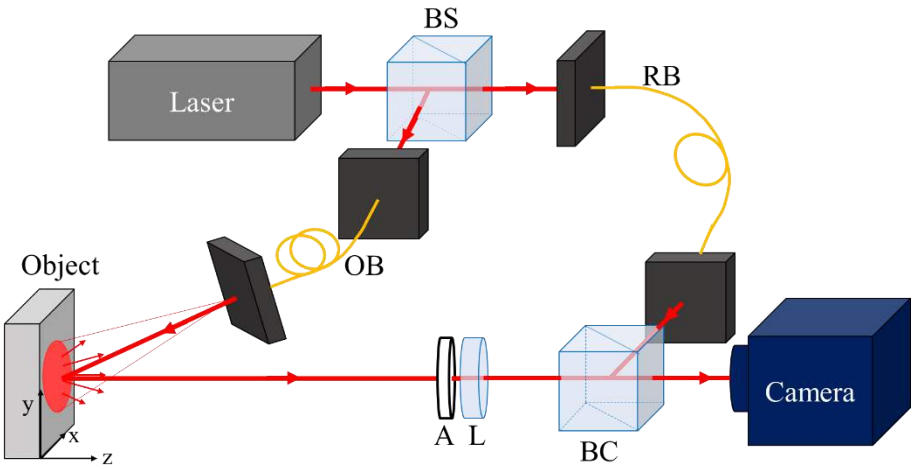

Figure 5. Schematic view of a DHI setup with an out-of-plane sensitivity.

The relevance of retrieving the optical phase difference lies in the information about the relative change of the object coming from a physical parameter during the recording process. The Fourier method is widely used to obtain the optical phase information for a single off-axis image hologram, which could be used for a later comparison with a second hologram. The recorded intensity for an image hologram is given by:

$$I(x,y) = a(x,y) + b(x,y)\cos\varphi, \qquad (2.13).$$

here, the (x,y) terms indicate the pixel coordinates on the camera's sensor, $a(x,y)$ and $b(x,y)$ are the background signal and the modulation factor, respectively. The term φ is the optical phase information contained in one image hologram, while $\Delta\varphi$ will be the optical phase difference between two image holograms. Equation 2.13 can be rewritten as

$$I(x,y) = a(x,y) + c(x,y) + c^*(x,y), \qquad (2.14)$$

with

$$c(x,y) = \frac{1}{2}b(x,y)\exp(i\varphi(x,y)), \qquad (2.15)$$

and $$c^*(x,y) = \frac{1}{2}b(x,y)\exp(-i\varphi(x,y)). \qquad (2.16)$$

Where terms $c(x,y)$ and $c^*(x,y)$ contain the phase difference information. In order to filter this information contained in the image hologram, a Fourier Transform is applied to equation (2.14):

$$\mathcal{F}\{I(x,y)\} = A(u,v) + C(u,v) + C^*(u,v). \quad (2.16)$$

The (u,v) terms represent the coordinates on the spatial frequency domain of the image hologram. Since DHI uses a spatial carrier method, both terms, $C(u,v)$ and $C^*(u,v)$ are spatially resolved in the frequency domain, as it is shown in Figure 6. The term $A(u,v)$ represents the DC term present in the system that contains the low-frequency variations along with the background noise signal. By filtering the term $C(u,v)$ and then calculating its inverse Fourier transform, $c'(x,y)$, it is possible to obtain the optical phase for a single hologram [62]. This method also works when $C^*(u,v)$ is selected, but the phase values will be inverse (-1) to those obtained with $C(u,v)$.

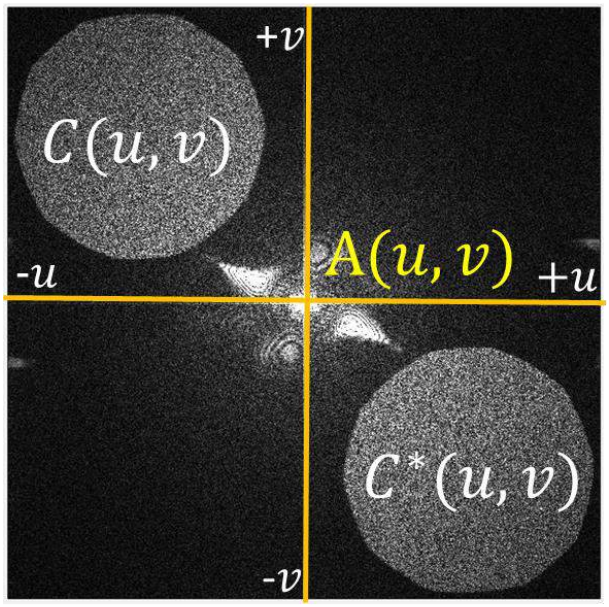

Figure 6. Example of a Fourier spectrum from an image hologram.

As it was mentioned before, DHI, as a two-state technique, needs two image holograms recorded at different times for reference, I_r, and the modified, I_m, states. From these states, the relative optical phase difference is obtained by using the following expression [61]:

$$\Delta\varphi = \text{atan}\left[\frac{Re(c'_r)Im(c'_m) - Im(c'_r)Re(c'_m)}{Im(c'_r)Im(c'_m) + Re(c'_r)Re(c'_m)}\right], \quad (2.17)$$

where c'_r and c'_m are the inverse Fourier transform of the filtered phase terms from the reference and the modified holograms, respectively; Re and Im denote the real and imaginary parts of the complex values obtained after the spectral filter. A general schematic view to obtain the phase difference $\Delta\varphi$ is presented in Figure 7.

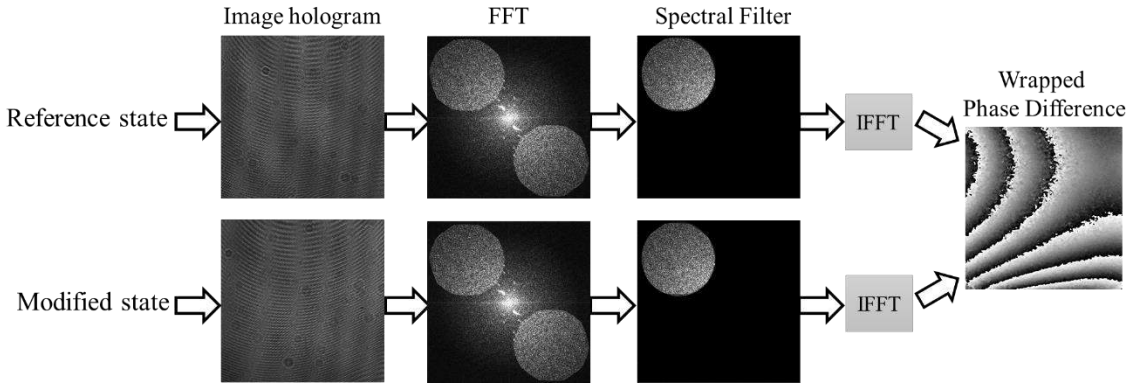

Figure 7. Sketch example to obtain the relative optical phase difference from two holograms.

From Figure 7, a wrapped optical phase map $\Delta\varphi$ is retrieved. This map has values between $-\pi$ and π due to the domain of the trigonometrical inverse tangent function (atan). So, an unwrapping algorithm is used to obtain a smooth optical phase $\Delta\varphi'$ when needed. Once the unwrapped phase map is retrieved, it can be used to obtain a displacement of the object through the sensitivity vector [63].

$$\Delta\varphi' = \frac{2\pi}{\lambda}\boldsymbol{s}\cdot\boldsymbol{d}, \tag{2.18}$$

where λ is the illumination's wavelength, d is the displacement, and $\boldsymbol{s}$ is the sensitivity vector that depends on the setup geometry. The displacement over the surface is measured in the direction of the sensitivity vector; for an out-of-plane configuration, the displacement is along the z-axis, ~ perpendicular to the object's surface.

2.1.6 Transmission Digital Holographic Interferometry

The information obtained with DHI under different kinds of tests provides essential data that produces a dynamic and continuously evolving field of research. Nevertheless, most of these studies are devoted to opaque samples where their surface is analyzed. Recent advances involve the analysis of transparent or semi-transparent samples with a configuration that avoids the sample's illumination in line with the camera's sensor [64], as it is usually set with a Mach Zehnder interferometer. With this modification, parasitic background patterns, speckle noise, and illumination saturation are effectively eliminated.

Considering the out-of-plane DHI configuration shown in Figure 8a, the object and reference beams are directed by the optical fibers OF1 and OF2, respectively. The camera's sensor collects the backscattering from the opaque illuminated object. However, if the object is transparent and is situated along the object's beam, it is possible to have a projection of it (see Figure 8b). Here, the object is replaced by a Neutral Phase Screen (NPS) illuminated by the object beam. The NPS must be solid and optically stable to avoid the introduction of any spurious optical phase. Then, the sample is placed between the NPS and the OF1 output. The system will detect any change within the sample that generates an optical path difference as an optical phase difference over the NPS. With this configuration, the object arm of the interferometer is working in transmission mode, and the camera's sensor detects the phase variation over NPS. This method is called transmission digital holographic interferometry (t-DHI).

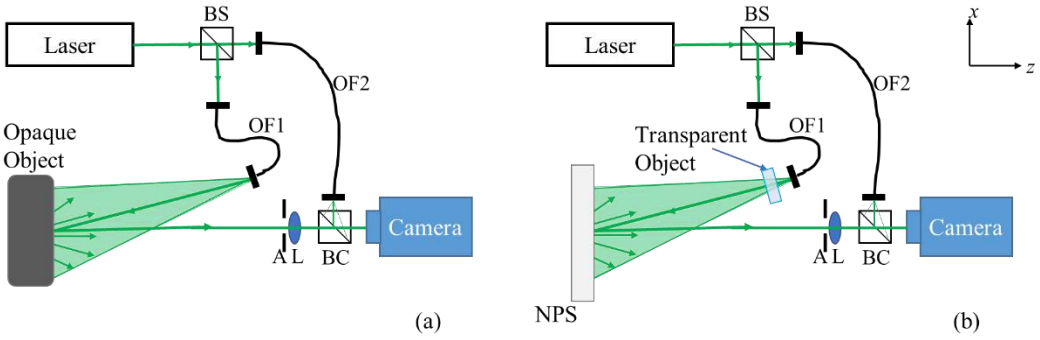

Figure 8. Schematic view of an (a) out-of-plane and a (b) transmission DHI system.

The t-DHI configuration can adjust the magnification factor by modifying the distance between the OF1 output and the sample; the latter modifies the size projection over the NPS, which is convenient for analyzing small samples in a simple form [33]. However, it has limitations for large transparent media, where the illuminated area of the sample is extended to improve the system's sensitivity. Here, the object arm is expanded and collimated, as presented in Figure 9. This characteristic allows the detection of any disturbance in large transparent media sections [17,34]. Since the OF1 output illuminates a concave mirror (cM) at its focal length, the reflected beam determines the illuminated area of the sample due to the mirror's diameter (collimated). In this configuration, the transparent media has no magnification over the NPS. Please notice that the angle between the collimated beam and the observation directions is complementary, as it cancels the geometrical distortion (the Schematic of Figure 9 does not show this condition).

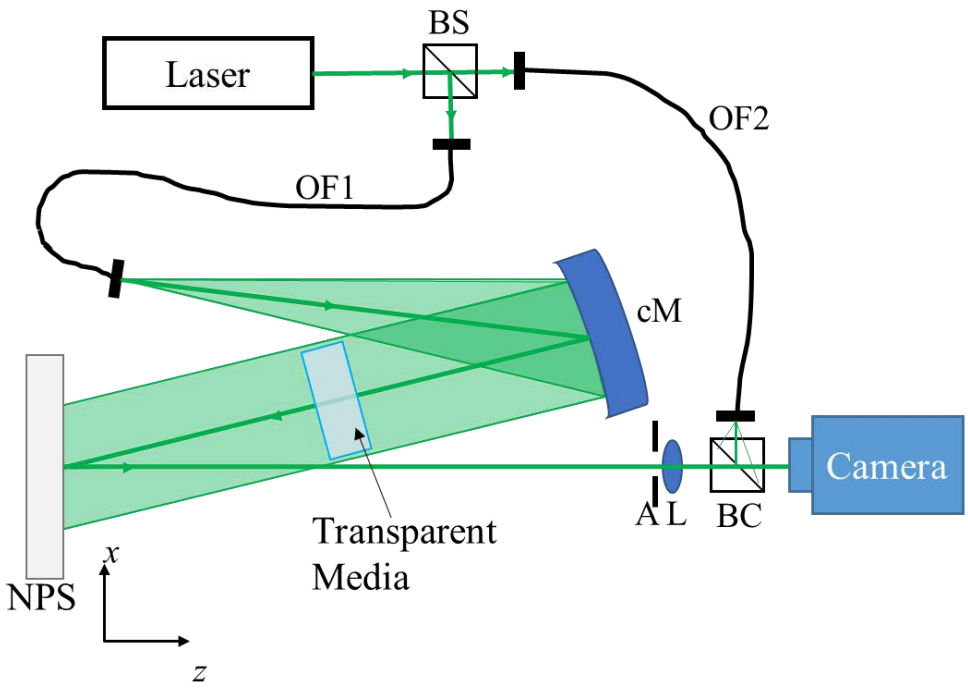

Figure 9. t-DHI system with a collimated object beam.

As the t-DHI method uses the projection over the NPS as the observed object, retrieving the optical phase difference between two states of the sample described for an out-of-plane configuration is valid for the transmission mode (equation 2.17). Besides, a displacement map can also be retrieved from the optical phase difference with the following expression,

$$w = \frac{\lambda \Delta\varphi'}{2\pi(1+\cos\theta)}, \tag{2.19}$$

where w is the displacement map along the z-axis, $\Delta\varphi'$ is the unwrapped phase difference map, and θ is the angle between the observation and illumination directions. The displacement can determine additional parameters related specifically to transparent media.

2.2 Optical Coherence Tomography

The Optical coherence tomography (OCT) method is a non-invasive, high-sensitivity interferometric technique that can inspect low-scattering media beneath the surface. It measures the reflected light that echoes inside the tissue, retrieving its internal structure. It is usually used in medical and ophthalmic fields to visualize the internal structure of biological tissues. Its working principle is based on interferometry, where the light source is divided into reference and object beams.

The most common OCT arrangement is based on a Michelson interferometer, as seen in Figure 10. In this setup, the OCT signal, which is the backscattered light from the sample, interferes with the reference beam. By using the characteristics of a broadband source, interference fringes are generated only when the light has traveled approximately the same distances in both arms of the interferometer within the coherence length of the source.

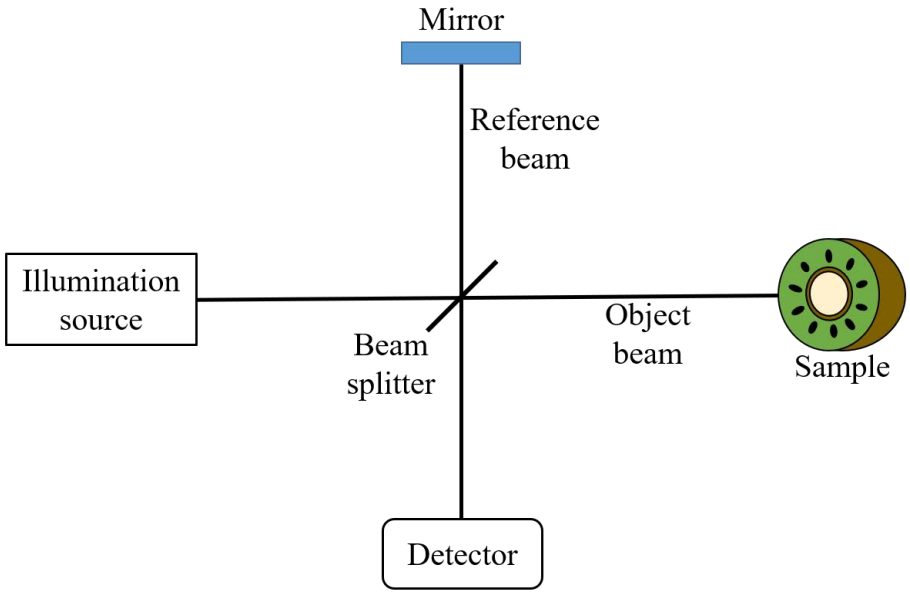

Figure 10. Schematic of a Michelson interferometer.

The coherence length determines the resolution and penetration capabilities of the optical system, l_c, given by

$$l_c = \frac{2\ln 2}{\pi}\frac{{\lambda_c}^2}{\Delta\lambda}, \tag{2.20}$$

where $\Delta\lambda$ is the bandwidth centered at a wavelength λ_c of the source. Medical OCT devices are typically centered at the near-infrared (NIR) band, making it common to find λ_c values at 840, 980, or 1300 nm. These wavelengths are widely used because they align with the

therapeutic window between 650 and 1300 nm [65]. Most body constituents like melamine, collagen, hemoglobin, and water within this range present minimal absorption and reduced scattering properties. These constituents are presented in low-scattering tissues relevant to ophthalmology, cardiology, dermatology, and gastroenterology. Consequently, the OCT signal is primarily formed by the backscattering coming from other structural materials in the sample that create the tomographic view of the object.

The backscattering waves from the object re-enter the OCT interferometer and travel with the reference beam until they overlap with the detector. At this point, the interference patterns of each wavelength are processed to construct the depth profile of the OCT tomographic signal. The interference signal in OCT can be divided into three types of scans: A, B, or C, according to the OCT setup. Figure 11a shows a schematic representation of OCT signal formation. An A-scan is created by illuminating a single point on the sample's surface, resulting in a 1D interference pattern converted into a 1D tomographic signal (A-scan of Figure 11b). However, for a B-scan, the sample is analyzed in a 2D depth profile by drawing a line on the object's surface of adjacent continuous A-scans (Figure 11c). The B-scan provides in-depth information from a sample slide. Finally, a 3D information set called a C-scan is produced with several adjacent B-scans (Figure 11d) [66].

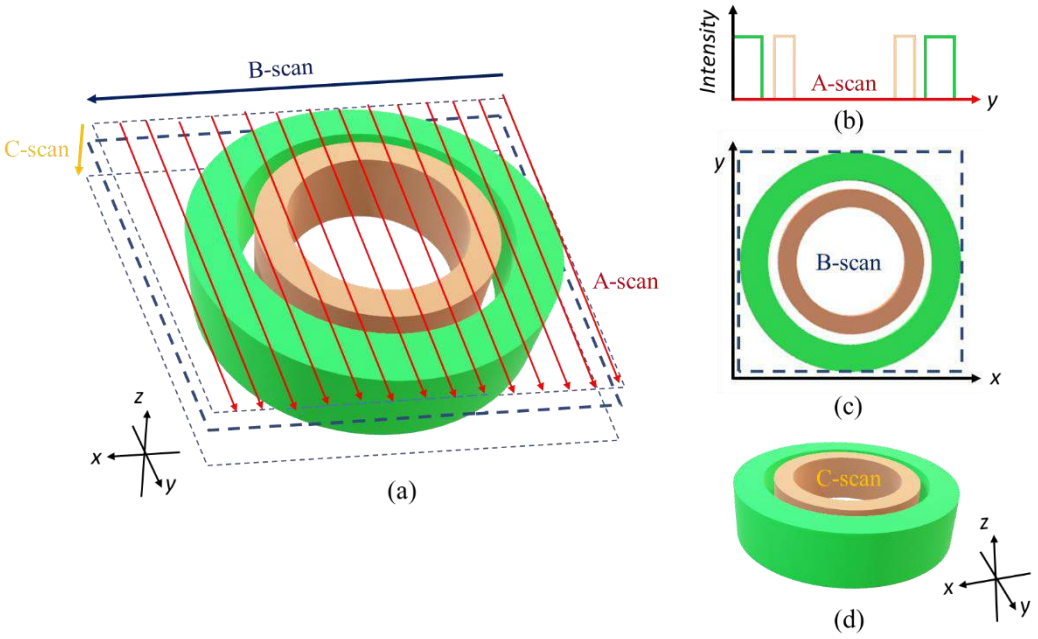

Figure 11. OCT (a) signal formations for (b) A, (c) B, and (d) C scans.

Since OCT relies on interferometry, the resulting interference can come from the illumination source emitting the entire bandwidth or only a portion at a time. Furthermore, the type of tomographic information available depends on the configuration used to collect the interference signal. The most common arrangements are the temporal, spectral, and quantum configurations.

Time-domain OCT (TD-OCT) configuration uses a Michelson interferometer associated with a single-point sensor. This setup involves modulating the reference length for each depth scan, and the intensity of the combined light at the sensor is recorded to generate the reflectance profile of the sample. Consequently, the sensor captures a 1D interference pattern. After recording this pattern, the system illuminates another adjacent point by moving the object (see Figure 12). This configuration requires synchronized scanning for the reference and the sample beam. This condition is represented in Figure 12 by the depth scan (reference) and the lateral scan (object) blue arrows.

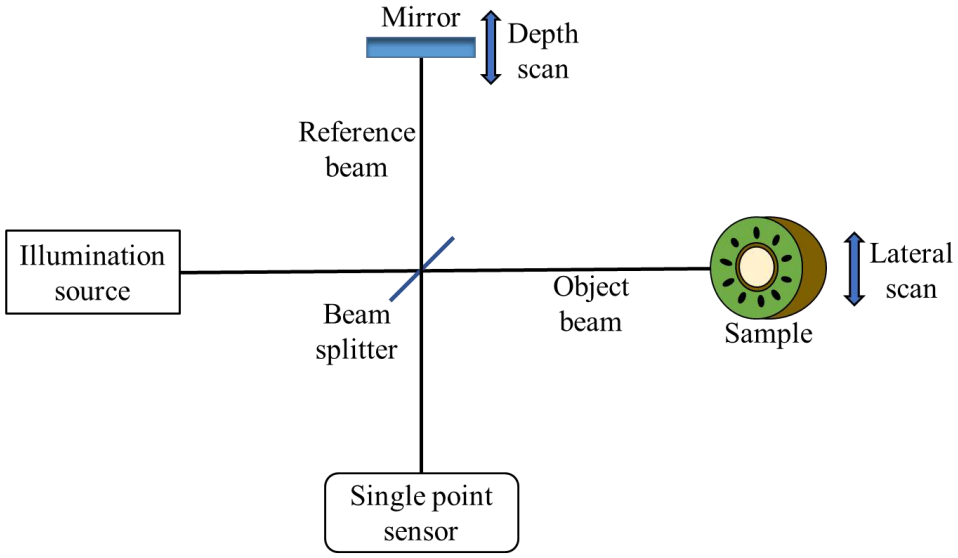

Figure 12. Schematic configuration of TD-OCT configuration.

On the other hand, the spectral-domain OCT (SD-OCT) configuration features a fixed reference arm. It employs a spectrometer to divide all the wavelength bandwidth into a line sensor, as presented in Figure 13. A diffraction grating in the spectrometer separates and resolves the optical source's bandwidth for a single point on the object. This setup requires a match between the grating's resolution and the size of the line sensor. In this configuration, the only scanning device is located within the object. The line camera captures the interference signal all at once, enabling the acquisition of an A-scan in a single exposure.

Modifying the optics and sensor of the SD-OCT configuration makes it possible to create a system that captures a B-scan in a single shot. This configuration incorporates a cylindrical lens that generates illumination across the object's surface (see Figure 14). This line has the entire bandwidth of the illumination source, enabling it to penetrate the sample in a 2D format. This configuration facilitates the recording of high-speed events due to the simplified A-scan recording process. Another advantage is the ability to rapidly reconstruct a C-scan by moving the sample or employing a tilting mirror in front of it. This method involves registering and stacking multiple B-scans to generate a C-scan efficiently.

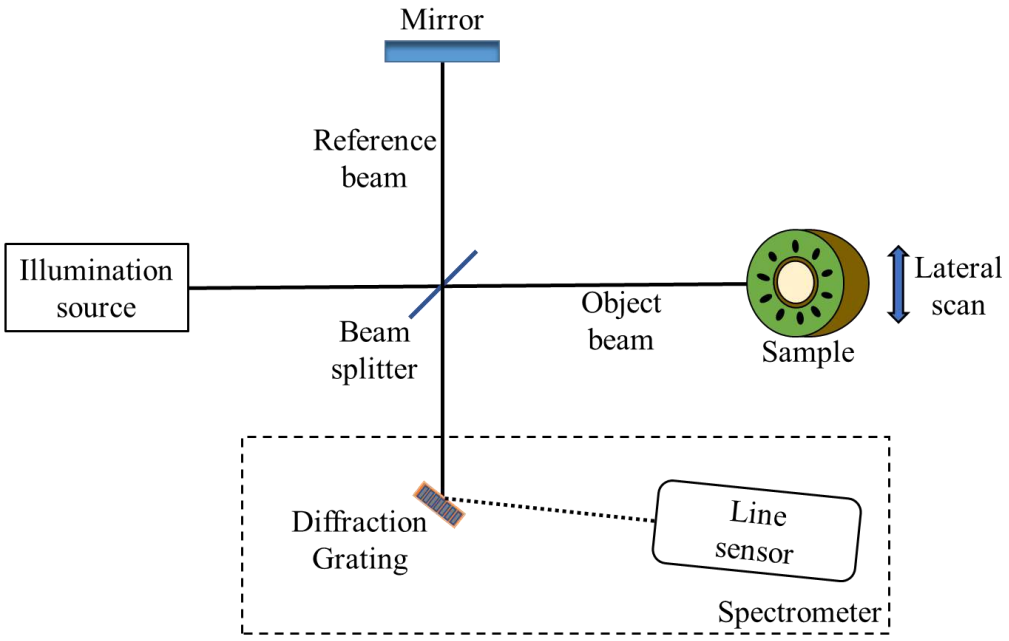

Figure 13. Schematic of an SD-OCT configuration. Here, the illumination source is split by a beam splitter into the reference and the object beams; both beams are diffracted by the diffraction grating and registered by the line sensor.

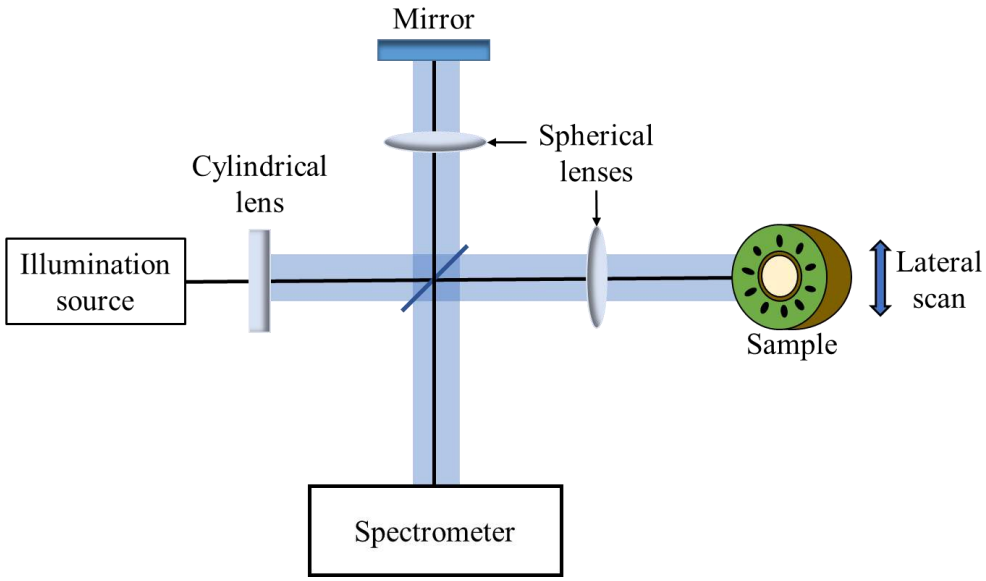

Figure 14. SD-OCT configuration for a single shot B-scan. Here, a cylindrical lens illuminates the sample's surface with a line; the spherical lenses focus this line on the spectrometer.

2.2.1 Fourier-domain OCT

A particular case of SD-OCT is the Fourier domain OCT (FD-OCT), where retrieving the optical phase between two tomographic images is possible. The Fourier transform uses the relative optical phase difference to detect inner mechanical changes affecting the object.

The interference signal registered by the FD-OCT configuration can be expressed as:

$$I(k) = I_0 + 2\sum_{j=1}^{M}\sqrt{I_R I_j}cos\big(\varphi_j(k)\big) + 2\sum_{i=1}^{M}\sum_{j=i+1}^{M}\sqrt{I_i I_j}cos\big(\varphi_i(k) - \varphi_j(k)\big), \quad (2.21)$$

where the first term, I_0, is the background or the DC term without phase; the second represents the consecutive interference between the reference beam, I_R, and the backscattering coming from the jth layer of the sample, I_j. The third term with a double summation means the auto-interference of the light coming from all the object slices, $I_i I_j$, where $\varphi_i(k) - \varphi_j(k)$ are the phase differences between light scattered from the i-th and the j-th slices. The optical phase, $\varphi_j(k)$, describes the structure of every layer with respect to the reference beam. When a Fourier transform is applied to an interference signal, these three terms can be identified in the spectrum [67].

As mentioned, this phase gives the relation between the backscattering light from different inner layers and a reference beam plane:

$$\varphi_j(\lambda) = \varphi_{j0} + \frac{4\pi}{\lambda} z_j, \quad (2.22)$$

where λ covers the entire bandwidth and goes from $\lambda_c - \Delta\lambda/2$ to $\lambda_c + \Delta\lambda/2$; φ_{j0} is the phase of the jth slice, and z_j represents the optical path difference between the reference plane and the jth slice. The latter can be expressed in terms of the wavenumber $k = 2\pi/\lambda$, as follows:

$$\varphi_j(k) = \varphi_{j0} + 2kz_j. \quad (2.23)$$

With the latter, the A-scan intensity is sampled uniformly along the k-axis; this process is known as linearization and avoids peaks broadening of the tomographic signal. The maximum optical path difference of the OCT system is represented by the depth range, Δz, which is limited by the spectrometer resolution:

$$\Delta z = N{\lambda_c}^2/4\Delta\lambda, \quad (2.24)$$

here, N represents the number of pixels used to sample the A-scan in the camera's sensor.

It is possible to determine the relative phase difference between two object states using the optical phase once the interference signal is in the Fourier domain. Here, each point layer inside the object has an associated frequency (*f*) depending on its depth,

$$f_{kj} = z_j/\pi. \tag{2.25}$$

This principle makes it possible to relate each f_{kj}, which contains the phase information of the j-th layer from different tomographic images to obtain a phase map as follows:

$$\Delta\varphi_j = \operatorname{atan}\left[\frac{Re\{\tilde{I}_1(f_{kj})\}Im\{\tilde{I}_2(f_{kj})\} - Im\{\tilde{I}_1(f_{kj})\}Re\{\tilde{I}_2(f_{kj})\}}{Im\{\tilde{I}_1(f_{kj})\}Im\{\tilde{I}_2(f_{kj})\} + Re\{\tilde{I}_1(zf_{kj})\}Re\{\tilde{I}_2(f_{kj})\}}\right]. \tag{2.26}$$

$\Delta\varphi_j$ is the phase difference up to the jth layer inside the object. $\tilde{I}_1(f_{kj})$ and $\tilde{I}_2(f_{kj})$ are the Fourier transforms of two processed A-scans at different times of the object deformation, and Re and Im are the real and imaginary parts of a complex number. The values of the optical phase lie between $-\pi$ and π, and an unwrapping algorithm will be used to obtain a smooth phase ($\Delta\varphi'_j$) when needed.

The phase difference between the two object states is evaluated in a single step by equation (2.26) by subtracting two tomographic images. Furthermore, the fringe pattern could be convolved with top hat kernels (apodization), which help to enhance the peaks' intensities when studying scattering materials and allow a maximum likelihood estimate of the phase difference [68]. A graphic diagram that describes the process to obtain the phase difference is presented in Figure 15.

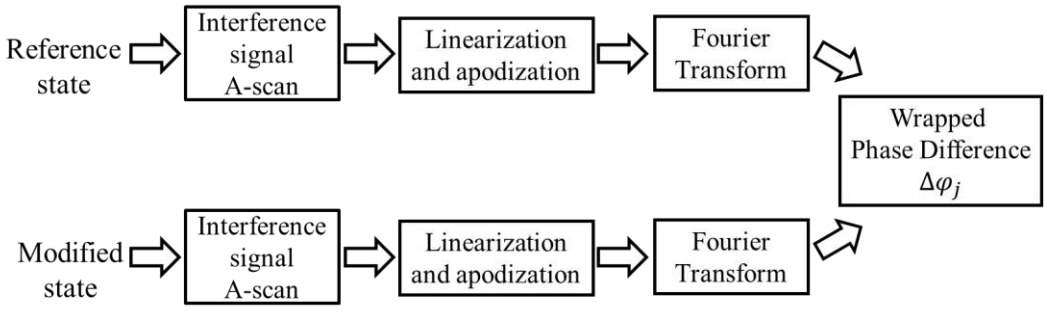

Figure 15. Graphic diagram to obtain the optical phase difference.

The unwrapped phase, $\Delta\varphi'_j$, can be related to displacements similar to those described in DHI (equation 2.19). However, as the FD-OCT illuminates the object in a perpendicular form, the relation is reduced as

$$w_j = \frac{\lambda_c}{4\pi}\Delta\varphi'_j, \tag{2.27}$$

where w_j is the resultant out-of-plane displacement component of the jth layer within the object. The phase sensitivity of the FD-OCT system will detect deformations smaller than the illumination wavelength; for example, a 2π phase change will represent $\lambda_c/2$ (half of the central wavelength of the broadband light source). For this reason, a more significant pixel number (*N*) in the sensor can detect smaller displacements with a smoother phase. Nevertheless, since each scattering point inside the sample is associated with a frequency, the object deformation must be small enough to prevent decorrelation in the phase. The latter requires a change of less than 2π at every pixel of the wrapped phase to obtain a useful displacement map that can be easily interpreted [66].

2.3 Fluid dynamics

The term fluid comes from the Latin verb "*fluere*," so fluids will flow. Liquids and gases are classified as fluids due to their ability to be easily deformed. A solid material maintains its defined shape unless there is a change in the external conditions. In contrast, a portion of fluid does not have a preferred shape, and different elements of a homogeneous fluid can be rearranged freely without altering the macroscopic properties of the fluid portion. When forces are applied, relative motion among different elements of a fluid portion gives rise to the field of fluid dynamics.

2.3.1 Equations of motion

Only flows of fluids where the continuum hypothesis is valid are considered. The latter means that the smallest volume of interest (a fluid element) always contains sufficient molecules for statistical averages to be meaningful [69]. In order to derive the continuity equation, the momentum equation, and the energy equation for fluids in motion, the principles of mass conservation, Newton's second law, and the conservation of energy are considered. The equations can be written in integral and differential form, either for large control volumes or for the motion of fluid particles, respectively.

The concept of flux refers to the flow of a physical quantity through a surface area of a control volume. For example, if a fluid has a particular density and temperature, these are carried across the surface with their momentum and energy. Consider the volume flux as the volume of all particles going through a differential area, dA, in the time Δt. For a three-dimensional, time-dependent flow, the velocity, $\mathrm{v}(x, y, z, t)$, and density, $\rho(x, y, z, t)$, are functions of three space variables and time (see Figure 16a). The volume, dV, that contains the fluid particles that pass through dA in time Δt, as represented in Figure 16b, can be identified by considering the average values of the distribution of ρ and v over the area as follows,

$$dV = (v\Delta t cos\theta)dA = (\mathbf{n} \cdot \mathbf{v}\Delta t)dA, \tag{2.28}$$

where $\mathbf{n}$ is the unit normal vector, which defines the orientation of the surface dA, the volume flux is defined as $(\mathbf{n} \cdot \mathbf{v})dA$, and the volume flux per unit area is represented by $\mathbf{n} \cdot \mathbf{v}$.

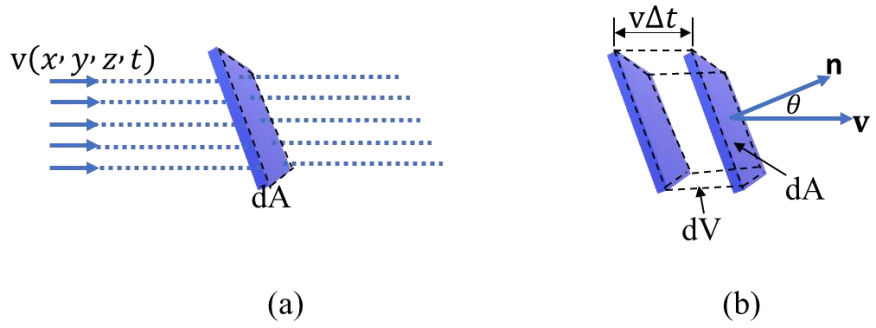

Figure 16. (a) Three-dimensional, time-dependent flow passing through dA, and (b) volume swept through dA in a Δt time.

Once the volume flux is defined, other fluxes can be easily set as follows:

- Mass flux: $\rho(\mathbf{n}\cdot\mathbf{v})dA$
- Momentum flux: $(\mathbf{n}\cdot\rho\mathbf{v})\mathbf{v}dA$
- Kinetic energy flux: $\frac{1}{2}(\mathbf{n}\cdot\rho\mathbf{v})\mathbf{v^2}dA$

2.3.1.1 Continuity equation

The conservation of mass requires that the difference between the mass flow rates entering and exiting a given control volume must match the rate at which mass accumulates within the volume. Consider the fixed control volume CV shown in Figure 17. When the flow is unsteady, the outflux and influx are unequal, so the mass inside the control volume may increase or decrease. From a fluid element of volume dV with mass ρdV, the mass of fluid inside the control volume at any time is $\int \rho dV$, hence, the rate of change of mass in CV is $\frac{\partial}{\partial t}\int \rho dV$. Furthermore, for a small element of surface area dA, the mass that flows outward across the surface is $\int \rho(\mathbf{n}\cdot\mathbf{v})dA$; here, the integrand will be positive when the flow direction is in the same direction as **n,** and negative when the direction is opposite to **n**. In the absence of sources of fluid, the mass of the fluid is conserved.

$$\frac{\partial}{\partial t}\int \rho dV + \int \rho(\mathbf{n}\cdot\mathbf{v})dA = 0. \tag{2.29}$$

Equation 2.29 is the integral form of the continuity equation for a fixed control volume in a three-dimensional, time-dependent flow. This condition can also be expressed in its differential form:

$$\nabla\cdot\rho\mathbf{v} = -\frac{D\rho}{Dt}, \tag{2.30}$$

where the divergence operator is defined as $\nabla = \left(\frac{\partial}{\partial x}, \frac{\partial}{\partial y}, \frac{\partial}{\partial z}\right)$.

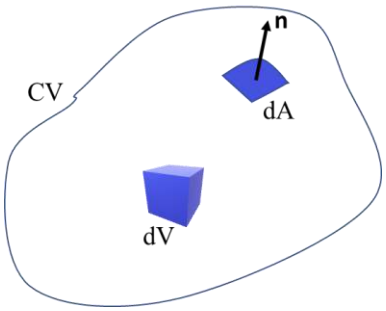

Figure 17. Fixed control volume for the derivation of the continuity equation.

There are three cases when equation (2.29) is simplified as follows:

$$\int \rho(\mathbf{n} \cdot \mathbf{v}) dA = 0. \tag{2.31}$$

The first case is when the mass inside the control volume is fixed, which usually implies a constant density. The second is for a steady flow, meaning the properties do not depend on time. And for the case of an incompressible flow. Considering an incompressible flow and the velocity vector perpendicular to the surface *dA*, equation 2.31 gives

$$\rho A v = \text{constant}, \tag{2.32}$$

and for a flow with constant density:

$$A_1 v_1 = A_2 v_2. \tag{2.33}$$

Equation 2.33 predicts that the speed varies inversely with the cross-sectional area for a steady incompressible flow.

2.3.1.2 Momentum equation

A fixed control volume is considered to derivate the integral form of the three-dimensional, time-dependent momentum equation. If a resultant force **F** acts on the fluid in the control volume, its momentum will change with time. This momentum can change in two different ways:

1. By a non-zero momentum flux over the control volume surface.
2. The unsteady momentum variation contained in the volume is due to the fluid variations in the density or velocity inside the control volume.

Unlike the conservation of the mass, the rate sum of change momentum in the control volume and the net outflux of momentum is not necessarily zero. The momentum is not conserved if a resultant force is acting on the fluid. Therefore, the momentum equation for a fixed control volume is given by

$$\sum \mathbf{F_{ext}} + \int \vec{\Sigma} dA + \int \rho \mathbf{g} dV = \frac{\partial}{\partial t} \int \rho \mathbf{v} dV + \int (\mathbf{n} \cdot \rho \mathbf{v}) \mathbf{v} dA. \qquad (2.34)$$

The first term on the right side of equation 2.34 is the rate of change of momentum inside the control volume (unsteady term), where the momentum of an element of volume dV is $\rho \mathbf{v} dV$. The total momentum contained within the control volume is $\int \rho \mathbf{v} dV$, and its rate of change is found differentiating with respect to time. This quantity is positive if the momentum inside the control volume increases with time. The second term represents the net outflux of momentum from the control volume (flux term) and depends on the surface area dA, which has a volume flux $(\mathbf{n} \cdot \mathbf{v}) dA$. The mass flux is given by $(\mathbf{n} \cdot \rho \mathbf{v}) dA$, and the momentum flux by $(\mathbf{n} \cdot \rho \mathbf{v}) \mathbf{v} dA$. On the left side of the equality is the resultant force that acts on the fluid. The term $\int \vec{\Sigma} dA$ represents the surface forces, $\int \rho \mathbf{g} dV$ the body forces and $\sum \mathbf{F_{ext}}$ are the forces due to external surfaces.

Surface forces include viscous forces acting over the control volume and forces due to pressure acting at right angles to the surface; if $\vec{\Sigma}$ is the surface force per unit area due to stress differences acting on the surface of the control volume, so its net resultant force is $\int \vec{\Sigma} dA$. Body forces include gravitational, magnetic, and electrical forces acting over all the fluid in the control volume. The only body force considered here is the force due to gravity, that for an element of volume dv with mass ρdV, is $\rho \mathbf{g} dV$; then its resultant force acting on the mass contained in the control volume is $\int \rho \mathbf{g} dV = m\mathbf{g}$, where *m* is the total mass. Finally, the forces due to external surfaces, $\sum \mathbf{F_{ext}}$ are the forces applied to the fluid by the walls of a duct, the surfaces of a deflector, or the forces acting in the solid cut by the control volume.

Equation (2.34) can be expressed in its differential form as,

$$\rho \frac{D\mathbf{v}}{Dt} = -\nabla p + \rho \mathbf{g} \qquad (2.35)$$

where ρ is the pressure over the fluid; this expression is often called the Euler equation for compressible and incompressible flows.

2.3.5 Navier-Stokes equation

Incompressible Newtonian fluids are governed by the Navier-Stokes equations, which combine the velocity vector field with a scalar pressure and consider viscosity's effects. The viscous force per unit volume is given by $\mu\nabla^2\mathbf{v}$, where μ is the viscosity coefficient [70]. This vector force per unit volume can be added to the Euler equation (eqn. 2.35), and we obtain

$$\rho\frac{D\mathbf{v}}{Dt} = -\nabla p + \rho\mathbf{g} + \mu\nabla^2\mathbf{v}. \tag{2.36}$$

This equation is known as the Navier-Stokes equation, and it is the momentum equation governing the flow of a viscous fluid.

The concept of a potential function is introduced, and it is relatively straightforward in a gravity field because of the related concept of potential energy, defining the following

$$\mathbf{g} = -g\nabla\psi, \tag{2.37}$$

where $\nabla\psi$ is a unit vector that points in the opposite direction of $\mathbf{g}$, the parameter ψ is a potential function and, in this case, is defined with the altitude. The quantity that measures the change in potential energy is the elevation, which is the potential function associated with the conservative force field due to gravity. Then, the Navier-Stokes equation for a constant property fluid becomes

$$\rho\frac{D\mathbf{v}}{Dt} = -\nabla p - \rho g\nabla\psi + \mu\nabla^2\mathbf{v}. \tag{2.38}$$

2.3.6 Bernoulli equation

The Bernoulli equation states that

$$p + \frac{1}{2}\rho\mathrm{v}^2 + \rho g\psi = \text{constant}. \tag{2.39}$$

This equation holds under steady, constant density flow conditions, with no losses along the streamline. It will also apply across streamlines if the flow is irrotational, that is, when $\nabla\cdot\mathbf{v} = 0$. The Bernoulli equation indicates that as the speed of a fluid increases, its pressure decreases, and vice versa, as long as the fluid is in a steady, incompressible flow and no external forces are acting on it. This principle is widely used in various engineering

applications, such as designing aircraft wings, calculating pipe flow rates, and understanding fluids' behavior in different contexts.

If points 1 and 2 are arbitrary points along the streamline, and considering a frictionless, steady flow of a constant-density fluid, the usual form of the Bernoulli equation is obtained.

$$\frac{p_2-p_1}{\rho}+\frac{1}{2}(\mathrm{v}_2^2-\mathrm{v}_1^2)+g(\psi_2-\psi_1)=0. \tag{2.40}$$

In fact, for an irrotational, inviscid, steady flow of a constant-density fluid, the Bernoulli equation applies between any two points in the flow field.

2.3.7 Reynolds-Number

The Reynolds number is a dimensionless quantity used to predict the flow regime of a fluid, whether it will exhibit laminar flow, turbulent flow, or a transitional state between the two. It is defined as

$$Re=\frac{\rho \mathrm{v} L}{\mu}, \tag{2.41}$$

where L is a characteristic length, such as a pipe's diameter or a rectangular duct's height. With this number, it is possible to predict the flow regime:

a) Laminar flow (Low Reynolds number). When *Re* is less than 2000, the flow tends to be smooth and orderly, with fluid layers moving in parallel. This response is typical in slow-moving or viscous flows.
b) Turbulent flow (High Reynolds numbers). As *Re* increases, the flow becomes chaotic and irregular, presenting eddies and swirls. Regarding Reynold's number, the flow is considered turbulent when Re exceeds 3500. Turbulent flow is typical at high velocity and low dynamic viscosity.
c) Transitional flow. There is a transitional range between laminar and turbulent flow where the flow behavior can shift from laminar to turbulent or vice versa. The transitions depend on surface roughness, flow disturbances, and specific fluid properties.

Turbulent flow is commonly observed in many natural and engineered systems, such as rivers, atmospheric air movement, and industrial pipes. However, it is a chaotic and complex type of fluid motion characterized by irregular fluctuations in velocity, pressure, and other flow properties. The study of turbulent flow is challenging due to its non-linear and highly unsteady nature, which leads to the lack of a general solution to the Navier-Stokes equations. Particular solutions exist, but they are not useful for the general understanding of the turbulent flow.

In order to deal with turbulence complexity, different approaches can be taken. The most common time-average approach is also called the Reynolds averaged approach. Here, turbulence is seen as a statistical phenomenon. It is assumed that the time-dependent nature

of turbulence is far too complicated to incorporate in a physical or turbulent model. Hence, the Navier-Stoke equations are written in terms of mean quantities using time averages, where a time average is taken over a long enough time to give a stationary mean. Hence

$$\bar{U}(x) = \lim_{T\to\infty} \frac{1}{T} \int_0^T U(x,t)\mathrm{d}t, \tag{2.42}$$

and

$$U = \bar{U} + u', \tag{2.43}$$

where $\bar{U}$ is the time-averaged velocity, as shown in Figure 18, and u' is a fluctuating field.

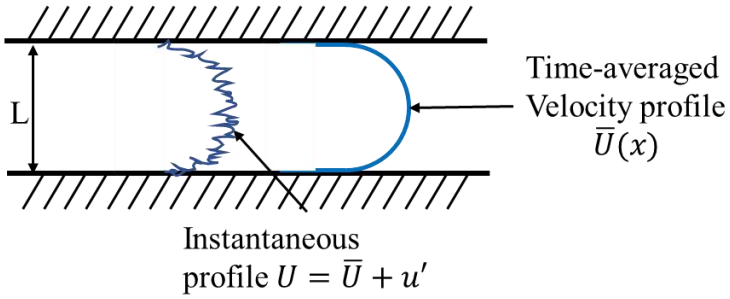

Figure 18. Instantaneous and mean velocity profiles in a channel flow.

The Reynolds-Averaged Navier-Stokes (RANS) equations are used in computational fluid dynamics (CFD) to simulate turbulent flows. They are derived from the Navier-Stokes equations, averaged in time. Here, an instant quantity is decomposed in its time-averaged and fluctuating quantities. For a steady flow of an incompressible Newtonian fluid, these equations can be written as follows.

$$\rho \bar{u}_j \frac{\partial \bar{u}_i}{\partial x_j} = \rho \bar{f}_i + \frac{\partial}{\partial x_j}\left[-\bar{\rho}\delta_{ij} + \mu\left(\frac{\partial \bar{u}_i}{\partial x_j} + \frac{\partial \bar{u}_j}{\partial x_i}\right) - \rho\overline{u'_\iota u'_J}\right]. \tag{2.44}$$

The left side of the equation represents the change in the mean momentum of a fluid element in the mean flow and convection by the mean flow. This change is balanced by the mean body force, the isotropic stress due to the mean pressure field, the viscous stresses, and the apparent stress ($\rho\overline{u'_\iota u'_J}$) due to the fluctuating velocity field.

2.4 Brief theory of bone structure and its mechanics

The bone is the main structural element of the skeletal system of vertebrates. It provides structural support, protects vital organs, and facilitates movement through muscular attachment. The bone is a remarkable composite structure characterized by a biphasic nature that includes an organic matrix and an inorganic mineral component. It is composed of three fundamental elements.

1) Fibrillary type I collagen that provides structural integrity

2) A mineral phase consisting of calcium-phosphate in the form of semi-crystalline hydroxyapatite to enhance strength

3) Water contributes to flexibility and resilience [71,72].

Combining organic and inorganic structures gives the bone lightness and resistance, classifying it as an intelligent material.

2.4.1 Hierarchical structural organization of bone

The hierarchical structure of all materials is fundamental, as it changes in dimensional scale, introducing distinct mechanisms of deformation and damage. For biological materials, this hierarchical organization is intrinsic to their design. This principle is exemplified in complex biological structures like bone, abalone shells, and crab exoskeletons [73]. The hierarchical structure of a bone is characterized by a sophisticated organization across multiple length scales, each contributing to performing diverse mechanical, biological, and chemical functions. These functions include providing structural support, protecting vital organs, storing healing cells, and maintaining mineral ion homeostasis. Understanding bone architecture requires the consideration of its intricate and hierarchical nature. In order to understand the mechanical properties of the bone, it is relevant to understand the properties of its constituent phases and their structural relationships across various hierarchical levels [74]. This approach is essential in comprehending the complexities of bone's mechanical behavior and functional adaptability. The levels and structures are.

1) The macro-structure: cancellous and cortical bone.

2) The micro-structure (10-500 μm): Haversian systems, osteons, and single trabeculae.

3) The sub-microstructure (1-10 μm): lamellae.

4) The nano-structure (a few hundred nm to 1 μm): fibrillar collagen and embedded mineral.

5) The sub-nanostructure (below a few hundred nm): molecular structure of constituent elements, such as mineral, collagen, and non-collagenous organic proteins.

All these structures (see Figure 19) have an irregular yet optimized arrangement and orientation, making bone a heterogeneous and anisotropic material [75].

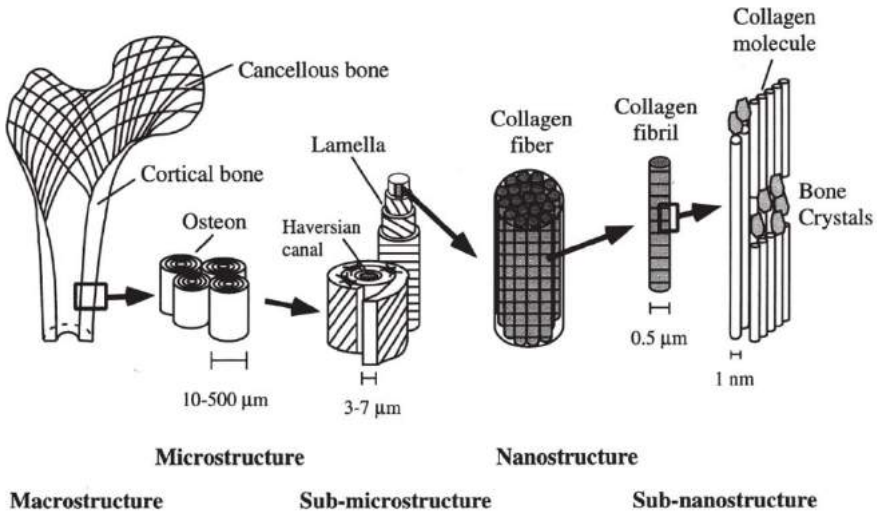

Figure 19. Hierarchical structural organization of the bone: (a) cortical and cancellous bone; (b) osteons with Haversian systems; (c) lamellae; (d) collagen fiber assemblies of collagen fibrils; (e) bone mineral crystals, collagen molecules, and non-collagen proteins. Image reprinted from [75].

Macrostructure

At the macrostructure level, bone is classified into two main types: cortical (or compact) and cancellous (or trabecular or porous) bones. For instance, the femur's end has a dense cortical shell surrounding a porous cancellous interior. Both types of bones can be distinguished by their porosity or density degree [76]. The microstructure of cancellous bone arises from its compaction, forming irregular, sinuous convolutions of lamellae. In contrast, cortical bone's microstructure consists of regular, cylindrical shaped lamellae.

Cancellous bone exhibits a higher metabolic activity than cortical bone. It is often remodeled, rendering it relatively "younger" on average. Therefore, although cancellous and cortical bones may share a similar material composition, their maturation process differs. The cortical bone's maturation can lead to microstructural alterations, impacting its mechanical properties.

Microstructure

The bone exhibits intricated arrangements of mineralized collagen fibers at the microstructural level, forming planar structures known as lamellae, typically 3–7 µm wide. The lamellae can be organized in concentric layers (3-8 lamellae), wrapping around central canals to form what is known as *osteons* or *Haversian* systems, resembling cylinders about 200–250 µm in diameter and aligned roughly parallel to the bone's long axis. In some cases, cortical bone may show woven patterns where mineralized collagen fibers lack alignment patterns, forming *woven* bone. Alternatively, lamellae in certain bone formations can run tangential to the bone's outer surface, creating a plywood-like stacking called *lamellar* bone,

often found alongside woven bone tissue and comprising thicker layers (150–300 μm) around the complete circumference of the bone.

Cancellous bone, on the other hand, consists of an interconnected network of trabeculae in various combinations. They all follow the basic cellular structures: rod–rod, rod–plate, or plate–plate. A trabecular rod typically ranges from 50 to 300 μm in diameter, contributing to cancellous bone's overall architecture and mechanical properties.

Sub-microstructure

The sub-microstructure of bone explores the composition and arrangement of bone lamellae, typically 3–7 μm thick, although the exact orientation within a lamella is not well known. Variations in lamellar organization may exist between cortical and cancellous bone. In the most accepted model, the collagen fibers within a lamella of an osteon are aligned parallel to each other, creating a structure similar to a twisted plywood or helicoidal pattern [77]. This model suggests that adjacent lamellae exhibit different orientations: longitudinal (with the collagen fibers along the long axis of the lamellar sheet) or transverse (with collagen fibers perpendicular to the long axis). These two orientations are alternated in sequential concentric lamellae, creating a spiral pattern around the central canal within an osteon. This complex arrangement of collagen fibers within lamellae contributes to bone tissue's strength, flexibility, and resilience, which are crucial in its mechanical properties and overall structural integrity.

Nano-structure

At the nanostructural level, the main structures observed include collagen fibers, which are surrounded and infiltrated by mineral deposits. While the precise attachment sites of macromolecules onto the collagen framework remain unclear, various immunohistological studies have indicated preferential labeling of specific macromolecules periodically along the collagen molecules and fibers [78].

Sub-nanostructure

At the sub-nanostructural level, bone contains three primary materials: crystals, collagens, and non-collagenous organic proteins. The mature crystals in bone are predominantly plate-shaped. These plate-like apatite crystals are situated within the confined spaces intercalated with collagen fibrils, which restricts their primary growth and results in discrete and discontinuous crystal formations. The average length and width of the plates are 50×25 nm with a thickness of 2-3 nm. The matrix's primary organic component is collagen, a triple helix structure with a diameter of approximately 1.5 nm, and is self-assembled to form fibrils. Non-collagenous organic proteins, including phosphoproteins, such as osteopontin, sialoprotein, osteonectin, and osteocalcin, may regulate the mineral deposits' size, orientation, and crystal habit.

2.4.2 Bone mechanical properties

Structure

As mentioned before, from a macroscopic point of view, there are two principal types of bone: cortical and cancellous. Cortical bone forms the outer layer of most bones and covers the shafts of large bones. Its low porosity contributes to its exceptional strength and stiffness compared to other bone types. Additionally, cortical bone shows a greater strength under compression than tension. The stiffness and resistance of cortical bone are influenced not only by the direction of the deformation but also by the deformation rate due to its viscoelastic properties.

Cancellous bone is found in the interior of vertebrate bones and at the epiphyses of large bones like the femur. Its high porosity gives it a lower strength than cortical bone but also significantly reduces its weight, making it much lighter overall. The pores also perform other physiological functions and contain the marrow. Thus, bone is an authentic multifunctional material. The structure of a long bone and a cross-sectional picture of a deer antler is shown in Figure 20.

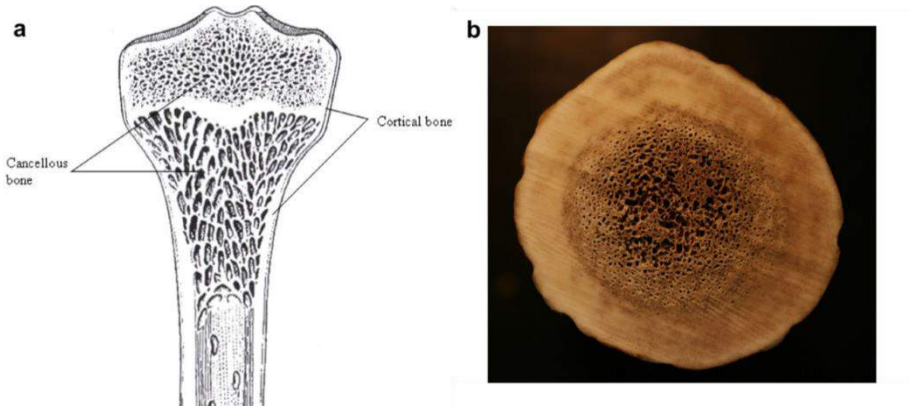

Figure 20. (a) Longitudinal section of a femur, and (b) a photograph showing a cross-section of deer antler. Image reprinted from [73].

Types of loads on bones

The skeletal system experiences various types of forces, so bones receive loads in different directions that try to change the shape of the material. These forces include principal or axial loadings of compression, tension, and shear (see Figure 21a). Compression is when an external force squeezes a material's molecules together. Tension occurs when the loads act to stretch or pull apart the material. Shear is a load applied at a right angle that acts in opposite directions. When multiple forces act on a body simultaneously, they can combine to create loads known as torsion and bending (see Figure 21b). Torsion refers to the twisting or rotational deformation of the material by applying torque or twisting forces. In bending, one side of the material experiences compression loading while the opposite side undergoes tensile loading. The immediate response of bone tissue to loads depends on various factors.

The size and direction of the forces, as well as their mechanical strength and shape, affect how the material's structure will change [79].

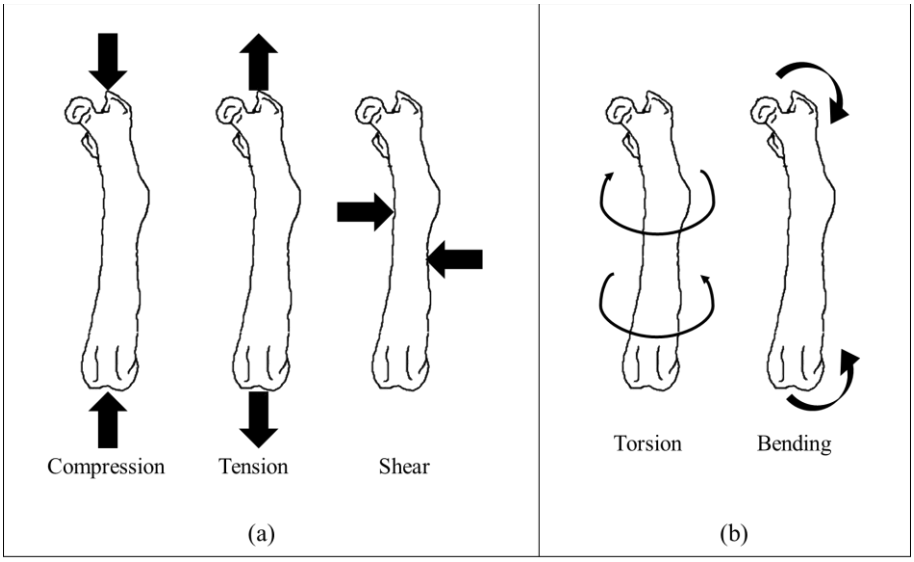

Figure 21. (a) Principal axial loads of compression, tension, and shear, and (b) combined torsion and bending loads.

The behavior of any material under different load conditions can provide insight into its properties, such as strength or toughness. When a material is subjected to a load, it experiences a force that deforms it. The force can be evaluated from the relation between the applied load and the material's deformation; this relation is known as the stress-strain curve.

Bone is a composite of collagen, hydroxyapatite, and water, a structure partially understood for its hierarchical structure. However, combining its fundamental materials gives the bone anisotropic and viscoelastic characteristics. Mechanical characteristics include anisotropy, viscoelasticity, elastic response, plastic response, fracture, and fatigue.

Anisotropy

The bone has an anisotropic behavior, which means that its mechanical response depends on the direction of the applied load. The strength and tensile/compressive moduli of bone along the longitudinal direction are greater than those along the radial and circumferential directions. Comparatively small differences in these properties have been observed in the radial versus circumferential direction, suggesting that cortical bone can be treated as a transversely isotropic material. The bone is strong enough to withstand loads in the longitudinal direction, as it is used to receive physiological loads in this direction [80].

Viscoelasticity

The bone also has a viscoelastic behavior because its mechanical response varies with the loading rate. During everyday activities, bone experiences strain rates ranging from 0.1 to 10% strain per second. The monotonic response of cortical bone can be assumed to have only a minor dependency rate. However, the stiffening and strengthening effects at higher strain rates are clinically significant. The latter is particularly relevant as impact loading can lead to strain rates exceeding ten times the physiological range. At higher strain rates, cortical bone tends to become more brittle, and the loading rate influences damage accumulation within the bone tissue [81].

Elastic response

The mechanical behavior of a material is studied by measuring the force and displacements of the material as it is deformed at various rates. A load-deformation curve is obtained, which can be converted with other measurements to obtain stress-strain graphs. These graphs have regions of interest, as presented in Figure 22. The elastic region is the initial linear region of the graph. If the test were stopped within the elastic region, the material would return to its initial shape. The bone exhibits elastic behavior when an applied load generates a deformation between 0 and 3%. The latter is the elastic amplitude of the load-deformation curve because the bone returns to its original shape once the load is removed.

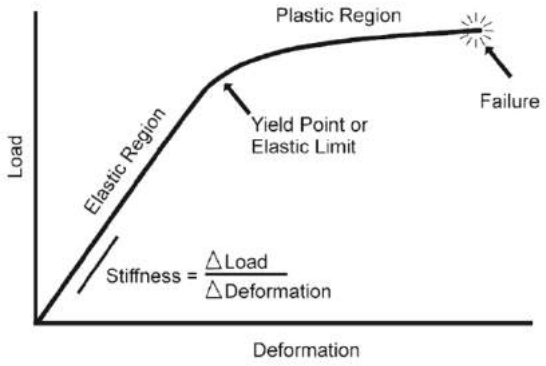

Figure 22. Regions and critical points in a load-deformation graph of an elastic material. Image reprinted from [79]

Plastic response

Beyond the linear region is the plastic region. If the applied load keeps increasing, the material will reach a deformation point that will not return to its initial dimensions. For biological materials such as bone, normal physiological loading occurs within the elastic region, and deformations beyond the elastic limit are associated with the degradation of the material properties (damage). Damage in bone has been defined in terms of the deterioration in the tissue microstructure or the nano-structure, collectively known as microdamage.

Fracture and fatigue

The mechanical strength of a material is the measurement of the maximum force the material can absorb before failure. When bones are subjected to applied loads, deformation will occur. However, bone fractures can occur from repetitive, subcritical loads (fatigue failure) or applied loads that cause local stresses that exceed the strength of the tissue [80]. A fracture is a disruption in the continuity of the bone. Many fracture morphologies in bone depend on the direction, magnitude loading rate, and duration of the mechanical load sustained, as well as the health and maturity of the bone at the time of the injury. Some examples are presented in Figure 23 [82].

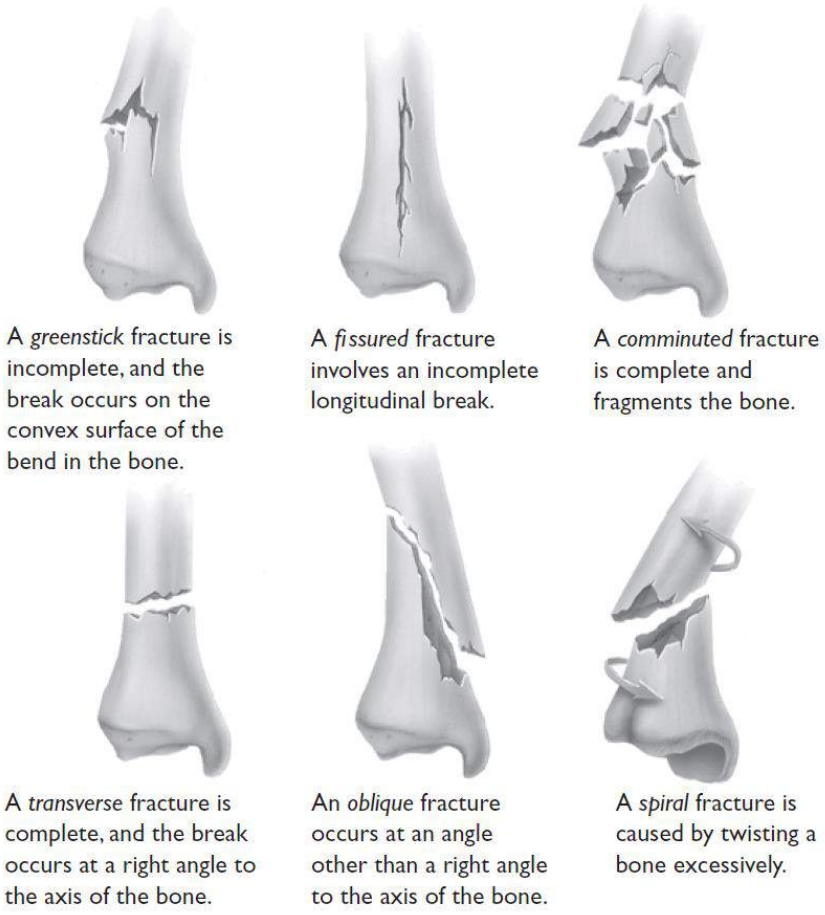

Figure 23. Six modes of fracture in bone. Image reprinted from [82].

The pattern and characteristics observed in a bone fracture provide significant insights into the nature of the applied forces and the underlying health of the bone tissue. For instance, a transverse fracture typically suggests a high-impact, perpendicular force, whereas

an oblique or spiral fracture may indicate an excessive bending and torsional load. Stress fractures often result from repetitive, low-intensity forces that cause cumulative damage over time. Additionally, the condition of the bone itself, such as signs of osteoporosis or other metabolic bone diseases, can be inferred from the fracture patterns. Analyzing these aspects helps understand the cause of the injury and promotes the development of preventive measures to protect the bone's mechanical health.

3. Experiments and results

This chapter presents the experimental methodologies used to analyze flow inside a water tunnel and study the impact on the mechanical behavior of mice's femoral bones due to storage media. According to the object under study, the results were obtained using interferometric techniques applied for transmission, surface, and internal analysis. For fluid dynamics observations, t-DHI was used, and for the mechanical analysis of bones (opaque and low scattered materials), out-of-plane DHI and FD-OCT were used simultaneously.

3.1. Fluid dynamics observation within a water tunnel using t-DHI

A wind tunnel is a demanding facility with complex processes and trained personnel for specific and costly tests. The hypothesis is to recreate a wind tunnel at scale but using a denser fluid. In this case, water was selected for its simplicity to produce a laminar and controlled flow. However, observing only water will not give information; for this reason, a transmission DHI system is used to detect flow variations. Consequently, conducting hydrodynamic tests on a scale model should yield flow lines comparable to those observed in aerodynamic tests conducted on full-sized objects.

As mentioned, DHI can detect disturbances in large transparent media such as water when modified in transmission mode [34]. This work applies a t-DHI setup to investigate the hydrodynamics within a water tunnel system. This system has a transparent chamber, allowing the observation of the interactions between the objects and the laminar flow that circulates in it. As proof of principle, three tests are presented: 1) Analysis of the water tunnel's flow without any objects in the chamber, determining whether the introduced water shows laminar or turbulent behavior. 2) A square plaque barrier blocks half the water's path to induce a flow change trajectory. 3) Introduction of a scale model car to observe its interaction with the laminar flow in the tunnel.

The retrieved optical phase from all tests makes possible the observation of hydrodynamic behavior comparable to those reported in the literature for simulations and experiments where the air is used (wind tunnel). The similarity between these two methods is possible in this scale water tunnel as the optical phase sensitivity requires micro water displacements to retrieve a displacement measurement. The proposed configuration in this work could be used as an alternative to aerodynamic tests in wind tunnels with the advantage of simpler compact hardware and, maybe, notably, a cost-reduced facility. The present section abords the development of the water tunnel system, its analysis with t-DHI, and the results obtained.

3.1.1 Water tunnel system

The final design of the water tunnel was made of five main sections: the water dispenser, the water distribution device (WD), the transparent chamber, the water recollection device (WR), and a water reservoir, as shown in Figure 24. This configuration was reached after several tests of different structures to have a controlled laminar flow inside the transparent chamber, taking into account the velocity of the flow, the area of the

transverse section through the system, and the position of the sections. Previous configurations are presented in Appendix A.

The transparent chamber is the section where the flow within is observed with the interferometer; for that purpose, it is made of thick transparent layers of PMMA (Poly-methyl-methacrylate) panels. It has dimensions of 500, 50, and 100 mm in length, width, and height, respectively (Figure 25a). The chamber is connected with the water distribution (WD) and recollection (WR) structures through rectangular clamps at both ends; the connection clamps have twelve holes each for the mechanical joint, as seen in Figure 25b. A rubber gasket is added to avoid leaks in the joints between the chamber and both terminal ends. The distribution water device uses eight water inlets of 1/2" in diameter, each, in four levels over the transversal section of the chamber. The latter is to obtain an entrance flow that is as uniform as possible. The same configuration is used for the water recollection. Also, a plastic grid block with square sections of 5 mm is situated at the beginning of the chamber to secure the direction of the injected water flow.

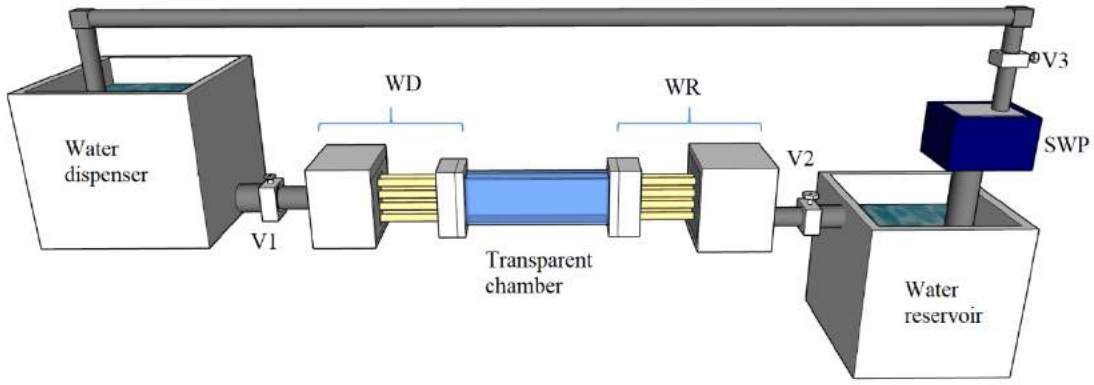

Figure 24. A schematic diagram of the water tunnel that indicates the height differences to promote water flow movement by gravity. The submergible water pump (SWP) is shown outside the reservoir for visualization purposes. V1, V2, and V3 are water valves 1, 2, and 3, respectively; WD and WR are the water distribution and recollection devices.

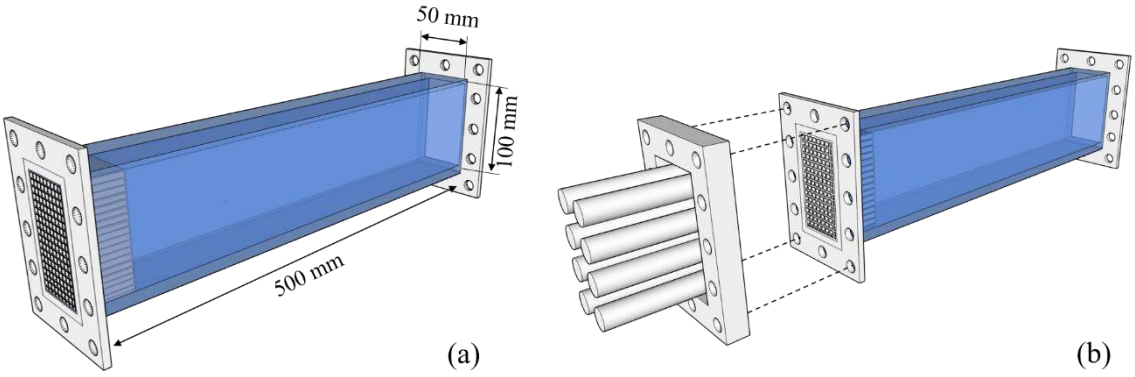

Figure 25. Digital design of (a) the chamber and its (b) joint with the distribution and collection structures using the rectangular clamps.

The water dispenser is a container with a maximum capacity of 20L connected to the WD. It is placed higher than the chamber since the system uses gravity to circulate the water. In order to have a controlled water flow inside the chamber, three control valves are used (see Figure 24). Control valve 1 (V1) allows the water to flow into the chamber; then, the water that passes through the camber is recovered by the WR and introduced into the reservoir, passing through the second control valve (V2). V1 and V2 help control the flow's velocity at both ends of the chamber; by adequately adjusting them, they produce a laminar flow inside the chamber. Then, a submergible water pump (SWP) brings the water back to the dispenser to close the water loop of the system. A third adjustable valve (V3) is connected to the pump to control the water transported back to the dispenser. These conditions, the water loop, and the dispenser's water level help maintain the same flow velocity in the chamber. The temperature of the tunnel water is constant as it is at room temperature.

3.1.2. Experimental set up for t-DHI

The schematic view of the optical system is shown in Figure 26a, and this setup is based on Figure 9, where a laser with a wavelength of 532 nm is used as the illumination source. It is divided by a beam splitter (BS) into a reference (RB) and an object (OB) beam, both coupled into single-mode optical fibers. The OB illuminates a concave mirror with a focal length of 1.55 m, such that the reflected beam is collimated, further illuminates the tunnel's chamber passing through it, and then falls on a Neutral Phase Screen (NPS). The NPS avoids introducing any spurious optical phase variation during the tests, such that any phase change observed is due to flow variations within the chamber. The backscattered light from the NPS is collected by an aperture-lens (AL) combination and imaged on the camera's sensor. The reference beam is added with the beam combiner (BC), generating an interference pattern on a PCO DIMAX-HD camera, set to capture images at 100 fps with a resolution of 1920 x 1440 pixels at 12 bits. As the concave mirror has a diameter of 250 mm, it limits the illuminated area of the transparent chamber. The observed region is selected to

avoid the grid block's end (see Figure 26b), resulting in an effective camera field of view (FOV) of 200 mm x 80 mm.

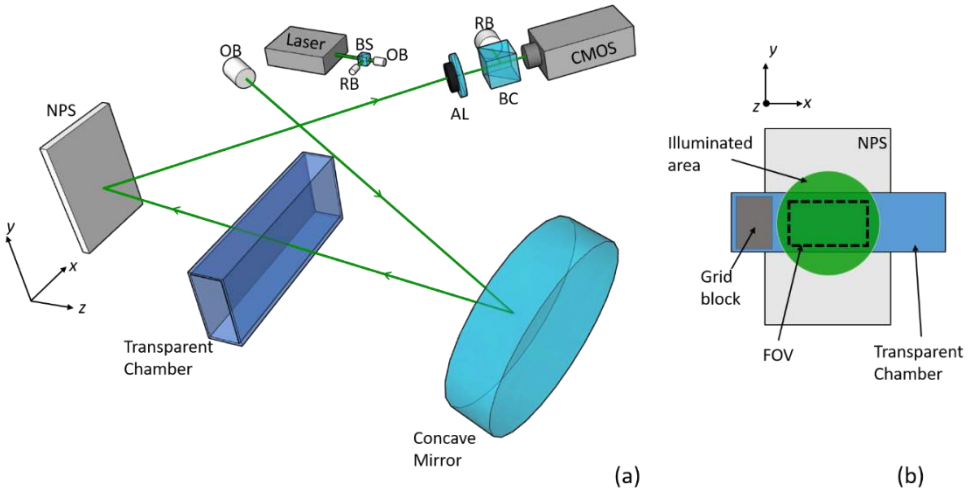

Figure 26. Schematic view of the (a) t-DHI system observing the water tunnel's chamber and (b) diagram of the observed region. RB and OB are the reference and object beams, BS is a beam splitter, BC is a beam combiner, NPS is the neutral phase screen, and AL is the aperture-lens combination.

3.1.3 Test with no obstacle inside the chamber

The water tunnel is placed in the object arm's path of the t-DHI optical system, taking care of any water licking on the optical table. As a precaution, a neoprene rubber cover is placed under the water system, as presented in Figure 27. The camera equipment and the laser are also waterproof protected.

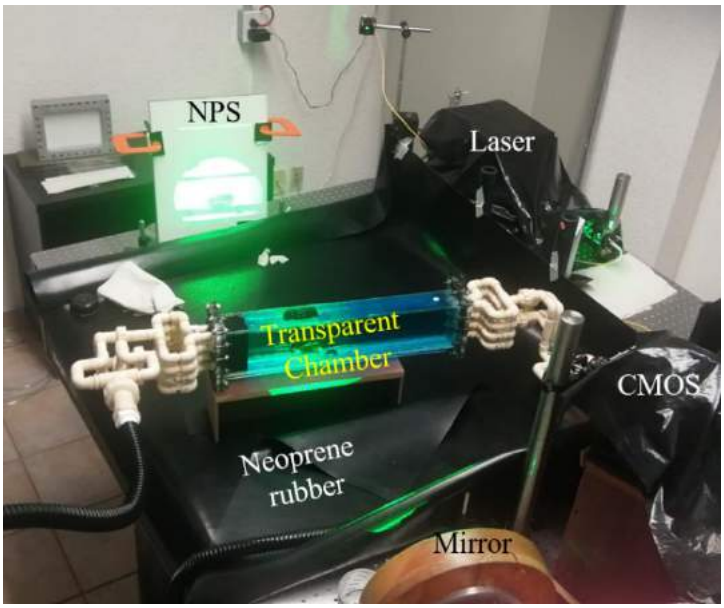

Figure 27. The water tunnel system is over the interferometric table and covered with neoprene rubber.

For all tests, the camera starts to record images, and then V1 is opened to let the water circulate inside the chamber. This condition means the tests pass from a water-static state to a dynamic one. The retrieved optical phase maps used an absolute reference state hologram throughout the experiment. The first experiment had no object inside the chamber since the objective was to analyze the interaction and advance of the incoming water with the static one inside the observation chamber. In Figure 28, a wrapped phase map, obtained with equation (2.17), is presented; this corresponds to an instant when the water enters from the left side of the image and advances in the chamber. Here, the four levels of the inlets are appreciable, and it is noticed that the water inside the chamber remains static until the water introduced reaches-interacts and moves it. The latter is validated with the optical phase as it appears to have zero magnitudes except in the inlet levels. The images correspond to a FOV of 200 mm x 80 mm for all cases.

It is possible to retrieve the displacement map from the corresponding unwrapped phase map (equation 2.19), as shown in Figure 29a. The displacement map is used to calculate the sparse vector field (see Figure 29b), where the arrow size is proportional to the vector's magnitude. Figure 29c shows a combined image of the displacement map and its corresponding sparse vector field. Observing Figure 29b and Figure 29c, the magnitude of the vectors is zero in regions where the liquid is static and increases where a flowing motion becomes present. The flow creates a displacement change proportional to the length of the arrows (which is proportional to the flow velocity) as the hologram is referenced to a static one with no displacement.

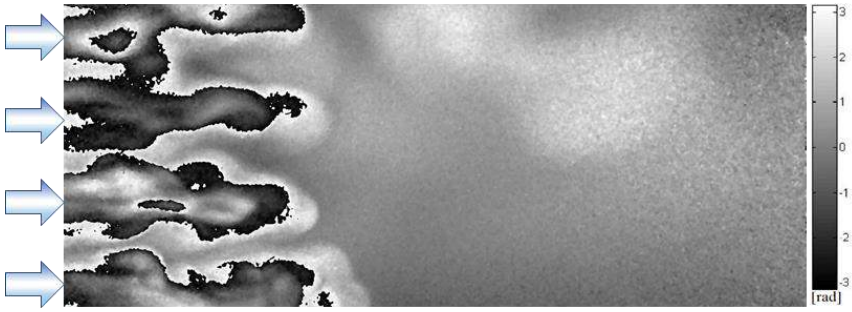

Figure 28. Wrapped phase map for an instant when the water from the inlets enters the chamber.

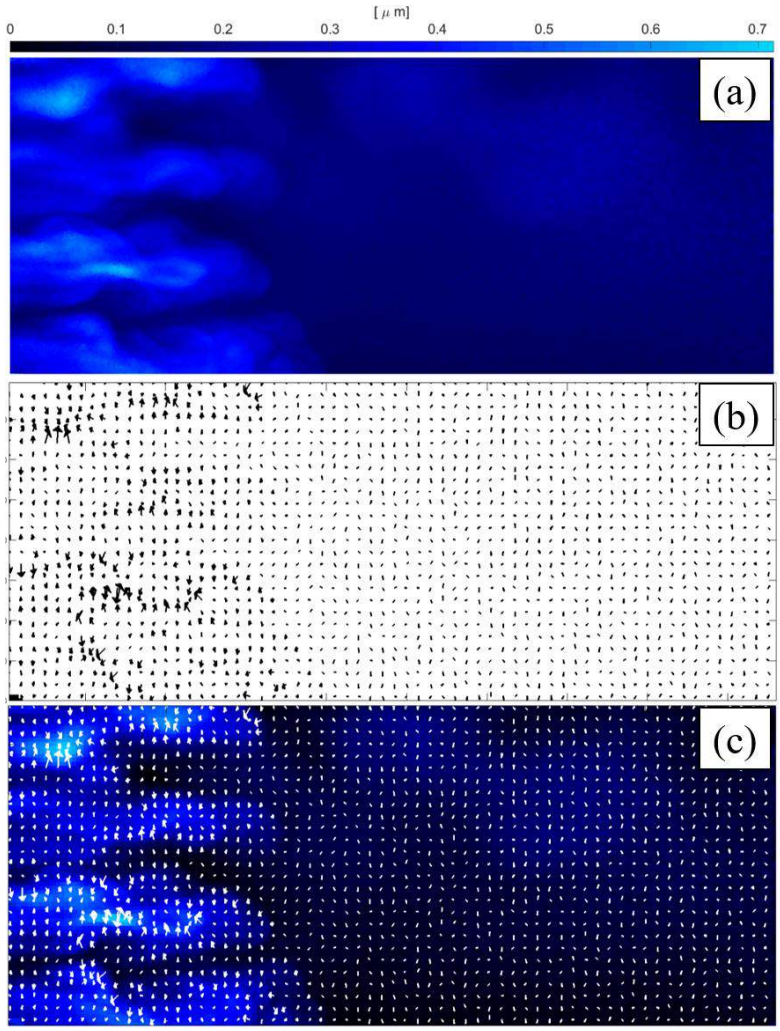

Figure 29. (a) Displacement map, (b) its corresponding sparse vector field, and (c) their combination.

Several tests were recorded referencing the holograms with a static state to determine the flow velocity as it advances through the chamber, with an average velocity of 11.3

mm/sec (for the experiments conducted here, it is considered a slow speed). Figure 30 presents a sequence of combined images (displacement and vector field) at different event instants: each one shows the displacement map and the sparse vector field.

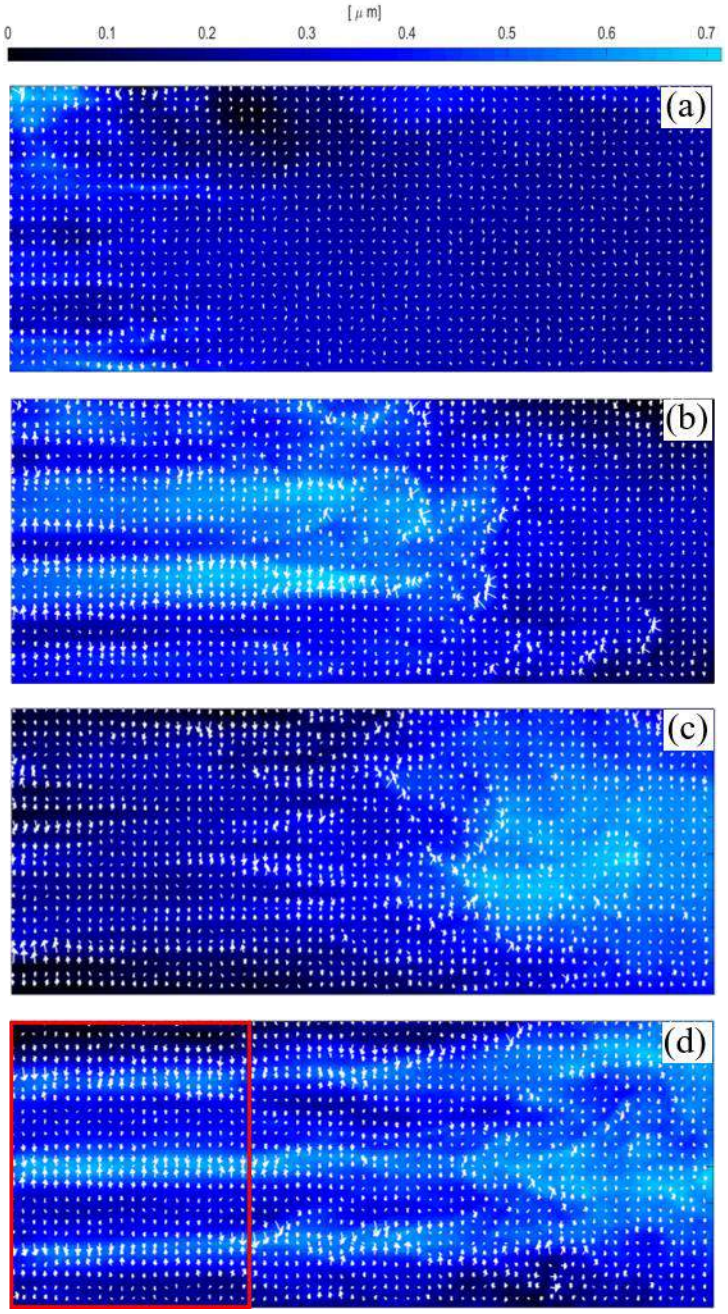

Figure 30. Combined images of the flow behavior in the chamber at selected times (a) 2.0, (b) 8.8, (c) 16.4, and (d) 24.4 seconds.

The optical system detects the water entering the chamber after 2.0 seconds, observed in a slight displacement variation with little changes in the gradient vector field, as Figure 30a shows. At this time, most of the water remains static inside the chamber since the entering water has not yet reached it. The displacement and the gradient vector field appear with no variations at the center and right-hand side of the registered FOV. The water keeps moving, and at 8.8 seconds, in Figure 30b, the liquid forms straight lines that match the inlet positions. In this region, the vectors point up and down, showing an outward displacement over the formed lines, indicating that changes are only for the incoming water with a steady velocity. However, minor turbulence is generated in the frontier of the introduced liquid and the chamber's stagnant water, showing arrows pointing to the left since the static water opposes the incoming water movement. Also, it can be noticed that the unreached water in the right observed section remains with no movement. The introduced water reaches the FOV's end in Figure 30c; small turbulences form at the right when both liquids find each other. Here, the vectors' orientation changes, indicating that flow replaces the steady state condition. Once the introduced water reaches the right side of the observed region (Figure 30d), the water trajectory appears straight (red rectangle) since there is no object to deviate from it. This behavior will be observed in the entire chamber as the water advances.

3.1.4 Barrier test

For the second test, a barrier that blocks half of the chamber's transversal section is placed to generate a forced deviation in the water trajectory. Figure 31 shows the schematic view of the barrier used for this test.

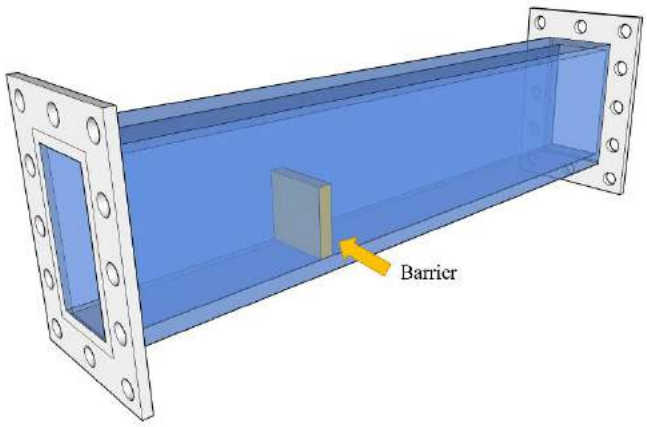

Figure 31. Schematic view of the barrier inside the chamber.

The same recording procedure used during the first test is applied; here, the camera starts to record images, and the valve is opened to let the water interact with the barrier. Figure 32 shows a time sequence of the displacement maps with their corresponding high-

density sparse vector field maps proportional to the flow velocity. The image sequence illustrates an evident alteration in the flow trajectory as the water is blocked and forced to pass through the upper section of the chamber. As expected, a turbulent flow is formed on the left side of the barrier during the test, generated by the impact of water against the structure.

As the water continues passing above the barrier, the deviation of the liquid initiates a swirling motion, as indicated by the green arrow in Figure 32b. However, the diameter of this eddy increases over time, as observed from Figure 32b to Figure 32g, while behind the barrier, the magnitude of its displacement (velocity) decreases with the progression of time. At the same time, the water flow over the barrier experiences a contrasting behavior (Figure 32e) since the displacement increases, generating a significant optical phase change while the swirl vanishes (see Figure 32h). Then, a static flow pattern trajectory is established over the barrier (Figure 32i to Figure 32j). This trajectory delineates the evolution of the water's movement over the barrier. It presents a stable and predictable flow pattern: the water impacts the barrier, passes above it, and continues along the chamber. Finally, the water at the back of the barrier remains static (green circle in Figure 32i) since the flow has been established over the barrier.

Figure 33 shows a set of combined images (displacement and sparse vectors) from the same results observed in Figure 32. Here, a low sparse vector field density improves the flow visualization. These combined images help to analyze the intensity and direction of the hydrodynamics in a single step.

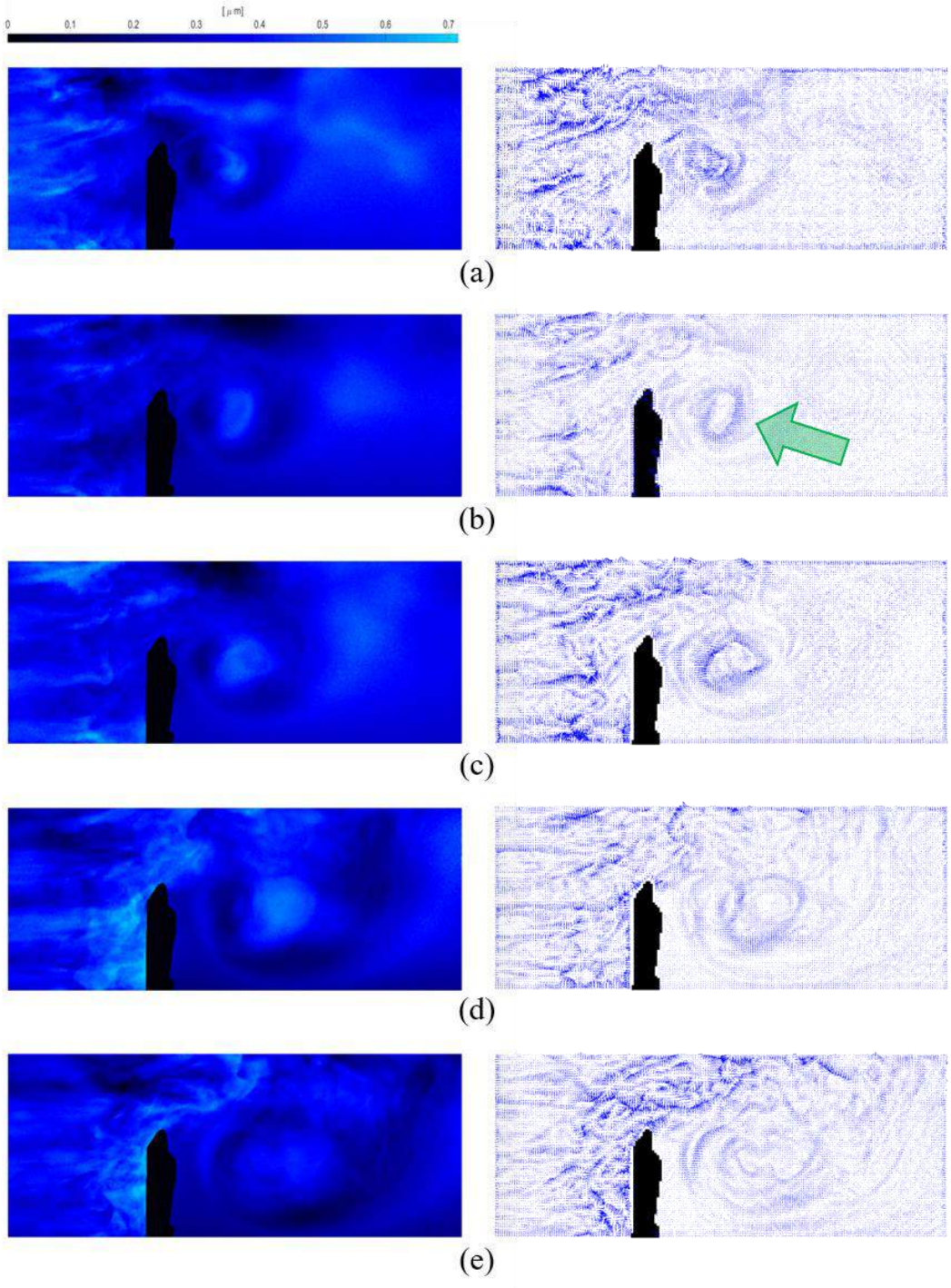
[μm]
0
0.1
0.2
0.3
0.4
0.5
0.6
0.7
(a)
(b)
(c)
(d)
(e)

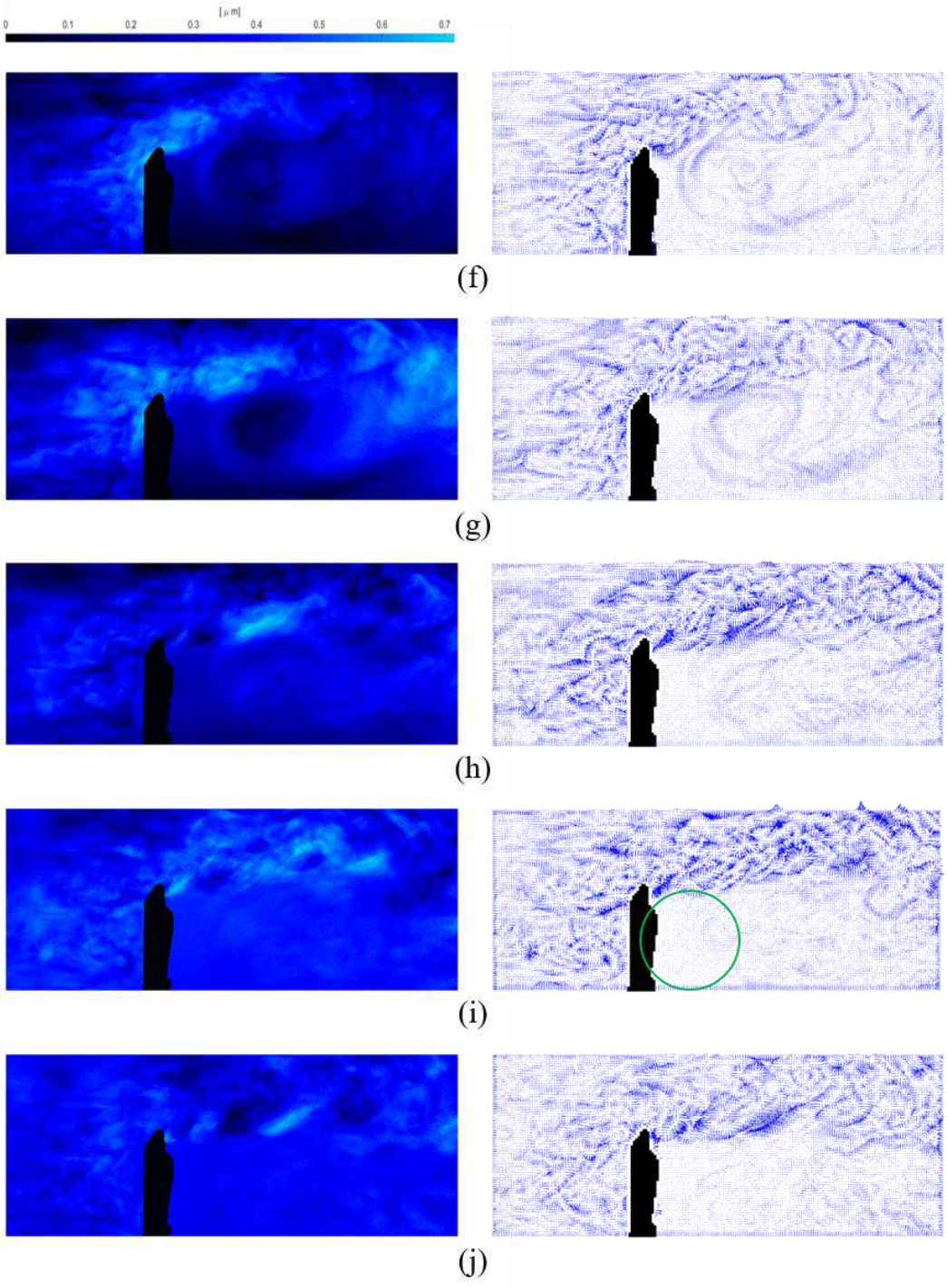

Figure 32. Examples of the hydrodynamic interaction recorded with the barrier at (a) 0.53, (b) 1.03, (c) 1.53, (d) 3.03, (e) 3.53s, (f) 4.53, (g) 6.03, (h) 6.06, (i) 6.53, and (j) 8.51 seconds. The green arrow indicates the swirl formation, and the green circle indicates the water that remains static.

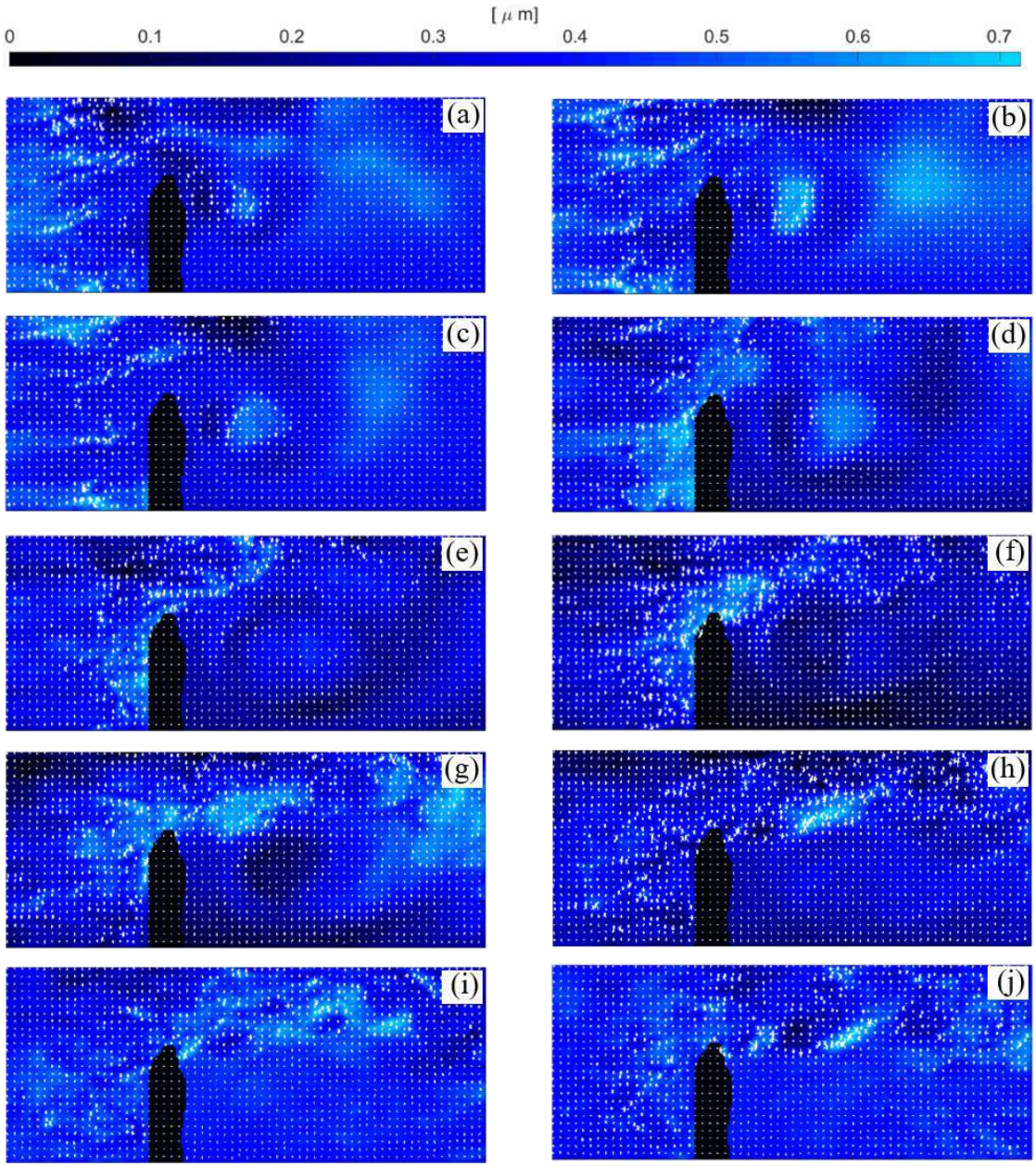

Figure 33. Combined images (displacement and sparse vectors) from the corresponding phase maps and vector fields shown in Figure 32. Notice that the obstacle is masked for display purposes.

3.1.5 Scale model car

For the third test, a scale hatchback car is situated inside the observable chamber and fixed to a platform using neodymium magnets. This fixation method ensures the mechanical rig does not introduce undesired flow changes. Considering the same experimental process described before, Figure 34 presents some instants of the flow interaction with the car model;

displacement maps and their corresponding high-density sparse vector field maps are shown. Figure 34a shows a remarkable difference from the behavior observed with the barrier in the previous test. Unlike the turbulence generated before the barrier, the model car deviates the introduced flow, which is an expected aerodynamic response. As the water flows through the tunnel, the optical phase exposes only a discernible drag effect behind the car. Figure 34b, Figure 34c, and Figure 34d show the drag effect at different instants. However, the drag remains constant once the flow is stabilized, as Figure 34d shows.

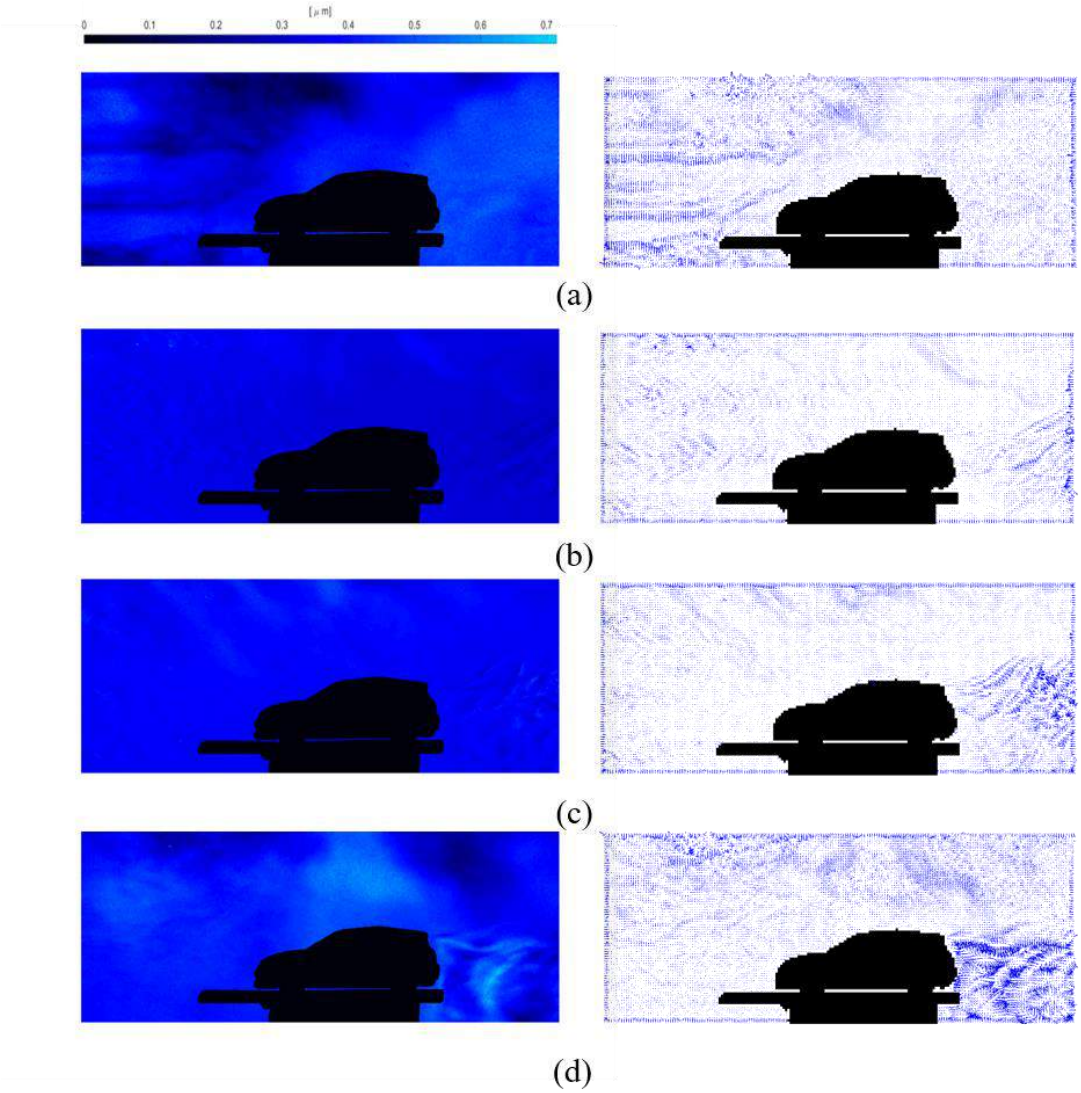

Figure 34. Hydrodynamic response for the scale model car at (a) 0.55, (b) 4.06, (c) 24.4, and (d) 60.4 seconds.

Similar to the previous tests, combined images are obtained for these instants, shown in Figure 35. From these images, it is possible to see the flow interaction with the model car. The visual representation shows a smooth interaction of the frontal section of the model car with the flow without turbulences, as the magnitude of the vectors is reduced dramatically in

this region of the chamber. This observation coincides with an expected aerodynamic behavior, where a controlled flow around the frontal section of a car is observed.

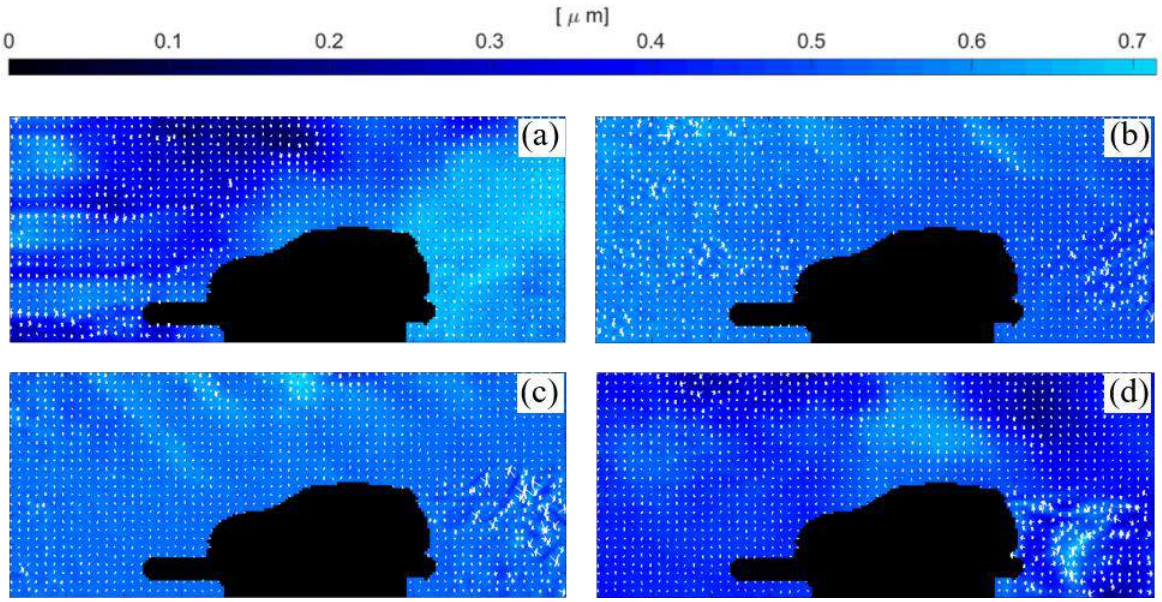

Figure 35. Combined images from the corresponding phase maps and vector fields in Figure 34.

Since the flow is laminar, the drag becomes visible, and the reference hologram has no phase changes at this point. The drag detection is accomplished by comparing the reference hologram with the deformed one. The water flow behavior observed during the present test could be comparable with results found in the literature for simulation and experimental results in wind tunnels. Some examples are when the fluid interaction is analyzed in a racing car during brake-in-turn maneuvers [83], where simulated streamlines were obtained. The results from the initial condition, before the car starts the maneuver, represent a comparable condition with the observed inside the water tunnel. Here, eddies are formed just after the rear window, and a drag effect is observed at the edge of the trunk. In both results (simulated and water test), the drag is formed and detected as turbulent flow lines, even when the simulated car is not a hatchback; this demonstrates a constant behavior for both types of vehicles. Another example presents the aerodynamic effect of a car's wings, where the airflow velocity contour around the vehicle is obtained with and without wings. In this case, eddies formations are also observed at the car's rear part [84], reinforcing the consistency of aerodynamic effects for different vehicle configurations.

An example of a simulation and an experimental test is found in reference [85], where a flow analysis around a sedan car is performed. This study uses tufts and digital cameras to capture the flow dynamics visually; here, the movement of the tufts matches the simulated flow distribution (see Figure 36). In both cases, eddies formation appears in multiple sections of the car. However, they are concentrated in the rear section, similar to the behavior observed in the water tunnel. The aerodynamic flow behavior registered in these reported works is similar to the results obtained with the proposed setup. However, using a scaled water tunnel

and t-DHI simplifies the experimental arrangement. Further processing is required to better represent the sparse vector field map with an attached color map to indicate the velocity instead of the dimension.

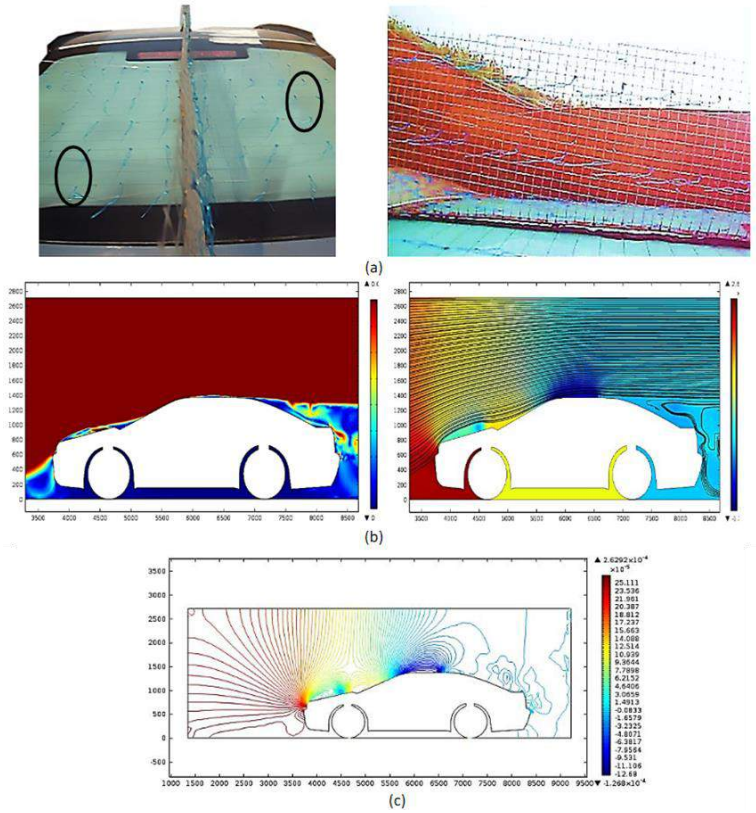

Figure 36. (a) Experimental results, (b) FSI, (c) CDF simulations for cruise speed of 80 km/h. Image reprinted from [85].

3.2 Impact of the storage media on the mechanical response of the bone

The most common solutions for hard tissue preservation, such as bone, are the saline and formaldehyde solutions [86,87] since they do not alter the material's mechanical properties in single-point experimentation. In order to assess the influence of the storage media on the viscoelastic properties of whole bone structure, a full field analysis of the deformation is conducted. For this purpose, during a mechanical three-point bending test, the bone's surface and internal deformation are monitored simultaneously using DHI and FD-OCT. As a comparison, Raman spectroscopy analyses these bones from different preservation media to prove that single-point inspection of the material is not affected as a whole field inspection.

3.2.1 Bone samples

The samples used for the mechanical testing were femur bones from wild-type mice (indicated in Figure 37). All possible efforts were made to minimize animal suffering. Previous works employing DHI in bone research have indicated a notable consistency in mechanical responses when observed with these methods. So, a reduced number of rodents is possible in these experiments. The experiments were conducted using adult wild mice of three months, weighing between 20-30 grams. All procedures were performed under the *Ethical Guidelines for the Use of Animals in Research* [88]. They were classified into three groups: fresh post-mortem (PM), saline (SS), and formaldehyde (FM) solution. The first bone group undergoes extraction and cleaning without any additional treatment. In contrast, after extraction and cleaning, the SS and FM groups are immersed in their respective solutions. All samples cover the universe of male and female femurs, with each case distinctly identified for comparative analysis (see Table 1).

The PM group is tested after extraction and has a surface drying period of 120 minutes to prevent specular reflections [42]. The SS and FM samples are immersed in their respective solutions for 48 hours post-extraction, followed by an identical 120-minute drying period before the actual test.

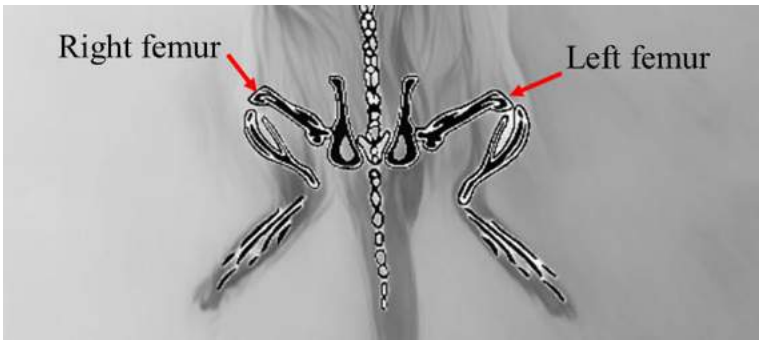

Figure 37. Schematic representation of the mouse skeletal, indicating the left and right femoral bones used in the test.

Table 1. Bones' classification by groups.

Preservation method		Fresh post mortem		Saline solution		Formaldehyde solution	
Gender		Female	Male	Female	Male	Female	Male
Code	***Left femur***	PM-F-L	PM-M-L	SS-F-L	SS-M-L	FM-F-L	FM-M-L
	Right femur	PM-F-R	PM-M-R	SS-F-R	SS-M-R	FM-F-R	FM-M-R

3.2.2 Three-point bending

All femoral bones were summited to a standard three-point bending (3PB) mechanical test, where a controlled displacement is applied until the fracture is reached. A schematic diagram of the 3PB is shown in Figure 38a. Here, the bone is placed and fixed to supports 1 and 2 with a separation of 12.5 mm. The applied displacement comes from a third point (3, in Figure 38a) employing a micrometric stepped motor (SM) with an attached tip centered between the fixed supports. The SM applies one step forward at a rate of 1.25 microns per step while both cameras of the dual setup (DHI + FD-OCT) capture images of the bone at a rate of 1.5 images per second, then, the SM applies another step, and both cameras re-record an image each. The SM continues applying the controlled displacement until the bone reaches the fracture (see Figure 38b). The full field surface and internal displacement maps are retrieved from these recorded images using the relative optical phase difference. The latter involves consecutive image holograms (re-referencing).

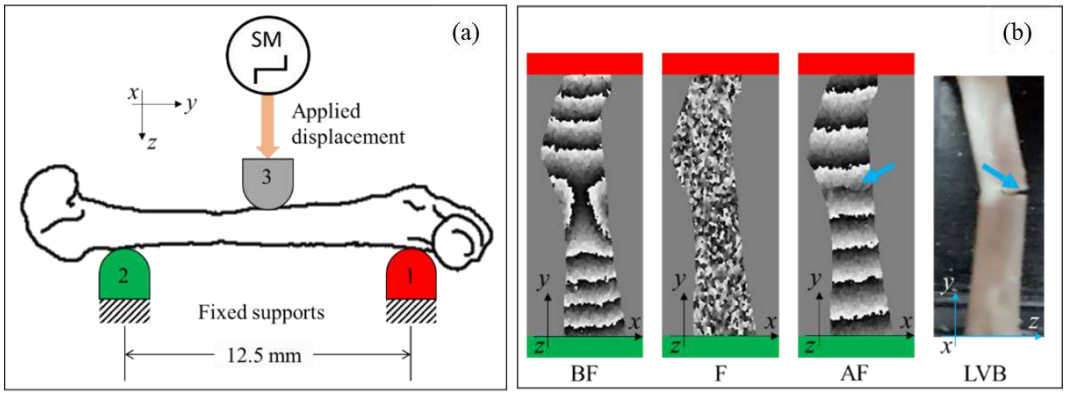

Figure 38. Schematic of the 3PB applied to the femoral bone, (a) showing the fixed supports 1 and 2 and the applied displacement point 3, (b) example of surface optical phase before (BF) and after (AF) the bone's fracture (F). A lateral view of the bone (LVB) shows this fracture. The front face of the femoral bone is the section observed by the optical setups. Blue arrows indicate the fracture position.

The 3PB test is widely used to determine the fracture, stress, and fatigue resistance of rigid materials under bending deformation [89]. It is generally applied to isotropic samples; the inherent two-state nature of optical methods allows for valid stepped deformation values in anisotropic samples such as bone [90]. The 3PB test is a standard tool for predicting and evaluating the mechanical response of materials for specific applications. Its simplicity makes it adaptable to various materials, including robust biological specimens like bone, offering valuable insights into their mechanical characteristics.

3.2.3 Raman spectroscopy setup

Raman spectroscopy is an analytical technique based on the principle of the Raman effect, which enables the examination of a specific point over a sample's surface to extract

detailed molecular-level information. This technique is employed to analyze vibrational, rotational, and other low-frequency modes based on the inelastic scattering of monochromatic light [91,92]. During the process, the frequency of photons changes as they interact with the sample, absorbing and re-emitting laser light. Raman spectroscopy provides a molecular fingerprint since the re-emitted photons' frequency shifts up or down with respect to the original monochromatic excitation source. In this context, Raman analyzes femoral bone samples preserved in different media. The Raman spectra were obtained from different surface points (spot size around 2 µm) of the femur with a Micro Raman system that uses an excitation laser of 632.8 nm and a microscope objective of 40X with a numerical aperture of 0.75. The Raman device was calibrated using the 520 cm^{-1} peak of a silicon wafer. Using a polynomial approximation, the Fluorescence background subtraction was performed with the OriginPro software (OriginLab Corporation).

3.2.4. Results

Observing the femoral bone samples during the 3PB tests requires that both setups are configured to capture continuous images during the applied displacements. Both techniques are aligned to focus on the bone surface where a common region is established as a shared region, as Figure 39c shows. The DHI system focuses on observing the *xy* plane of the anterior side of each bone, illustrated in Figure 39a. Simultaneously, the OCT system registers a tomographic image in the *zy* plane, aligned with the medial view, as depicted in Figure 39b. The tomographic image can record the cortical bone and marrow (indicated in light gray) along the minor axis, as shown in Figure 39b.

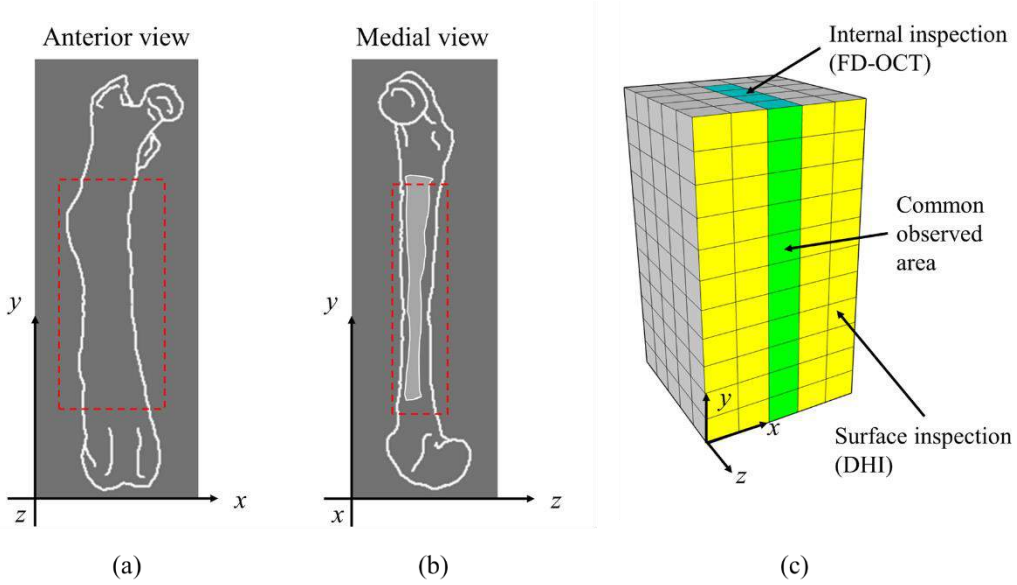

Figure 39. Bone's side observed by (a) DHI (surface) and (b) FD-OCT (one inner slice), (c) schematic example of a bone's section indicating the common observed area for both techniques. The short dashed red rectangle indicates the observed region of the bone.

A schematic view of the optical setup is shown in Figure 40a, where DHI and FD-OCT are represented as separate modules. The FD-OCT setup is placed at the bone's level while the DHI is above it. Both techniques observe the same bone's surface. The schematic diagrams of the DHI and OCT setups are presented in Figure 40b and Figure 40c, respectively. DHI uses a Cobolt Samba laser at 532 nm as a light source, which is divided into the object (OB) and reference (RB) beams using an 80/20 beam splitter (BS1). The object beam illuminates the sample, in this case, the anterior face (major axis) of the bone, whose backscattering is focused on the camera sensor C1 (Pixelink monochrome with 1280 × 1024 pixels) via an aperture (A) and lens (L1) with focal length 150 mm. The reference beam is combined with the object beam using a 50/50 beam combiner (BC). The FD-OCT setup is configured to obtain a B-scan in a single shot; it uses a Superlum broad lighter HP1module (SLD) centered at 840 nm with a bandwidth of 50 nm as the illumination source. This source is launched with the laser beam used in DHI (for alignment purposes) through an optical coupler (OC). One OC terminal is blocked (BT), while the other is collimated (CT) and directed to the setup. This beam is divided into the object and reference arms with a beam splitter (BS2). The object is illuminated with a line using a cylindrical lens (CL1) and a spherical lens (L2) with focal lengths of 150 mm and 100 mm, respectively. The object's backscattering is added to the reflected reference beam (passing through L3 with a focal length of 100 mm). Then they are diffracted by a blazed reflection diffraction grating (G) with 1200 lines/mm, which is focused on the camera sensor C2 (Pixelink monochrome with 1280 × 1024 pixels) with L4, a spherical lens with a focal length of 150 mm. The reference beam is reflected by a protected gold mirror (M1) and attenuated using a neutral density filter (NDF). The cameras C1 and C2 are two Pixelink monochrome imaging cameras.

For each test, the first step is the fixation of the bone, after which the optical systems start the image recording, and the SM moves the displacement tip until it reaches the back side of the bone. An optical phase change is observed at this point, and the applied displacement continues until each bone is fractured. Then, both systems stop recording, and a new bone is tested. The time to reach the fracture ranges between 3.7 and 5 minutes, depending on the preservation media and the gender. The approximated recording speed by each method is 0.7 frames per second. After all bones are tested, the optical information is processed with an algorithm that retrieves the optical phase for DHI and FD-OCT (equations 2.17 and 2.26, respectively). The fracture point is chosen from these images and serves as a shared reference for both methods and each bone. This approach facilitates the measurement of the displacement experienced by each bone since both methods are assumed to have the same recording speed. From this instant, several images previous to the fracture are considered to retrieve the temporal displacement applied by the SM. One hundred images are considered before the fracture to have the same period, making it possible to compare all bones directly. The resulting total deformation for this period is big enough to avoid speckle noise in both methods. In order to obtain the temporal (total) displacement, it is necessary to retrieve the stepped optical phases and apply a temporal unwrapping method. Figure 41 and Figure 42 show some continuous wrapped phase maps from each group and gender of the bones for the DHI and FD-OCT modules, respectively. For simplicity, the DHI optical phases show the right femoral bones, while OCT shows the left ones, as their corresponding pairs show similar results.

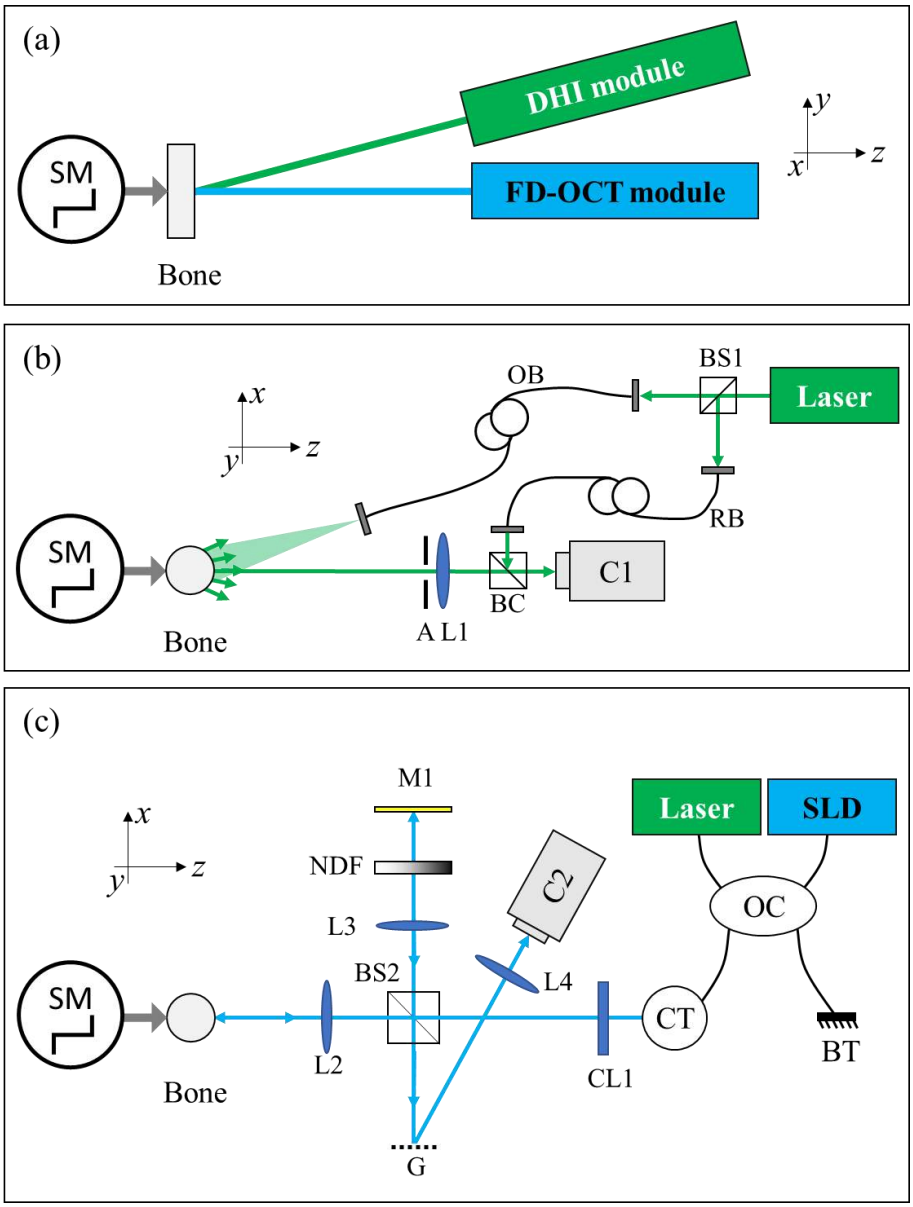

Figure 40. (a) Schematic view of the experimental dual setup showing each module position. Schematics of the (b) DHI and (c) FD-OCT modules. OB and RB are the object and reference beams. BS1 and BS2 are beam splitters. BC is a beam combiner; A is an aperture. L1, L2, L3, and L4 are spherical lenses, CL1 is a cylindrical lens, G is the diffraction grating, M1 is a mirror, C1 and C2 are the cameras, SLD is a super-luminescent diode, OC is an optical coupler, BT is a blocked terminal, CT is a collimated terminal, and NDF is a neutral density filter.

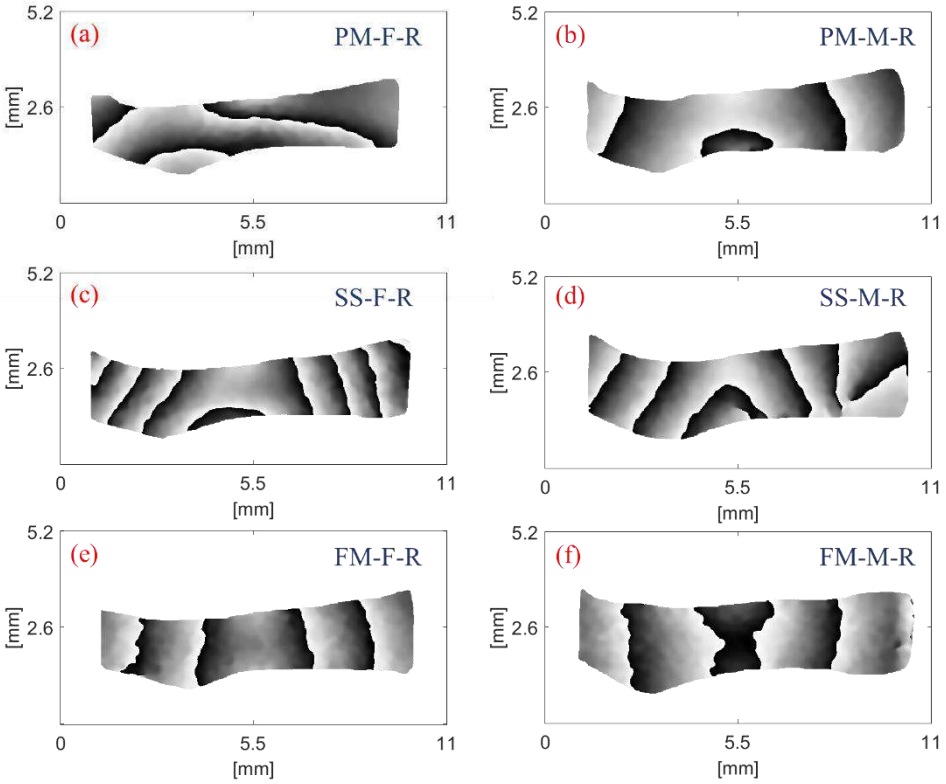

Figure 41. DHI wrapped phase maps from (a,c,e) female and (b,d,f) male femoral bones.

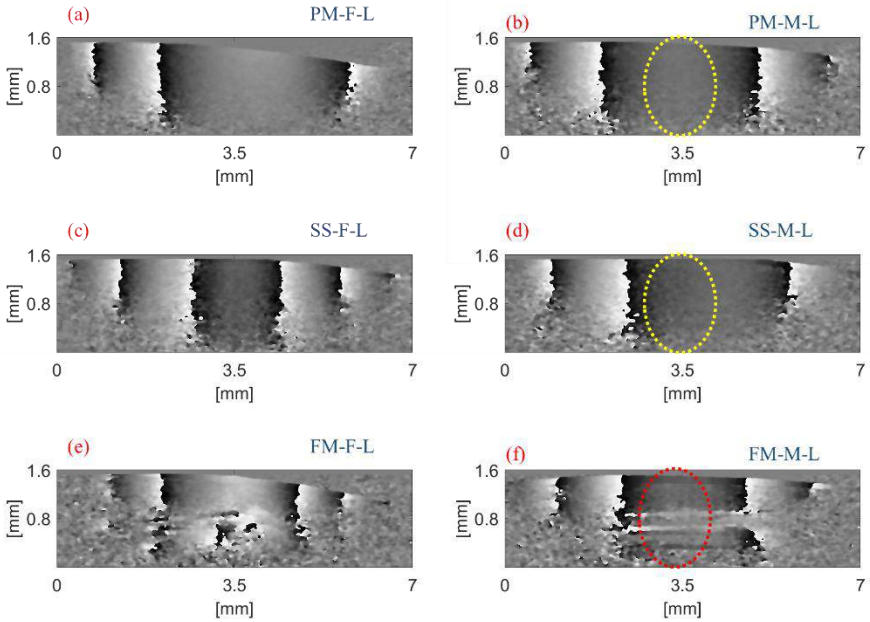

Figure 42. FD-OCT wrapped phase maps from (a,c,e) female and (b,d,f) male femoral bones. Yellow and red ellipses indicate the continuous and discontinuous phase response, respectively.

From Figure 41, it is possible to observe that DHI shows little phase differences when reference and deformed holograms are close in time. However, there is a remarkable difference between the FM group and the others. In the PM and SS groups, the optical phase describes a viscoelastic behavior that is asymmetric because it is not centered in the maximum deformation; actually, this maximum is found near the edges. In contrast, the formaldehyde bones display a uniform and symmetric distribution centered around the maximum deformation. This discrepancy has already been detected as a mechanical difference among the bone groups.

On the other hand, the internal OCT signal is smooth in the SS and PM bones; here, the marrow retrieves a continuous phase (i.e., yellow ellipse in Figure 42b and 42d). However, the formaldehyde affects the marrow as Figure 42e and Figure 42f show discontinuous regions observed as de-correlation patterns (for example, indicated with a red ellipse in Figure 42f). These discontinuities are present in female and male bones when formaldehyde is used. The FD-OCT signal decreases as the depth increases due to absorption. For this reason, the posterior side of the bone is not observed in these images.

After unwrapping all the DHI and FD-OCT phase maps, a temporal algorithm adds the stepped displacements to generate the corresponding full deformation map of the 100-image period. In Figure 43, the DHI maps for each group and gender are presented in pairs. Figure 43a, Figure 43b, Figure 43c, and Figure 43d show a fresh bone's typical anisotropy and viscoelasticity, where the bone’s structure continuously adapts as the SM’s tip moves during the test. Nevertheless, this pattern is significantly different in the formaldehyde bones, where a uniform and constant deformation is observed (Figure 43e and Figure 43f)—resembling more of an isotropic sample rather than an anisotropic one as the bone.

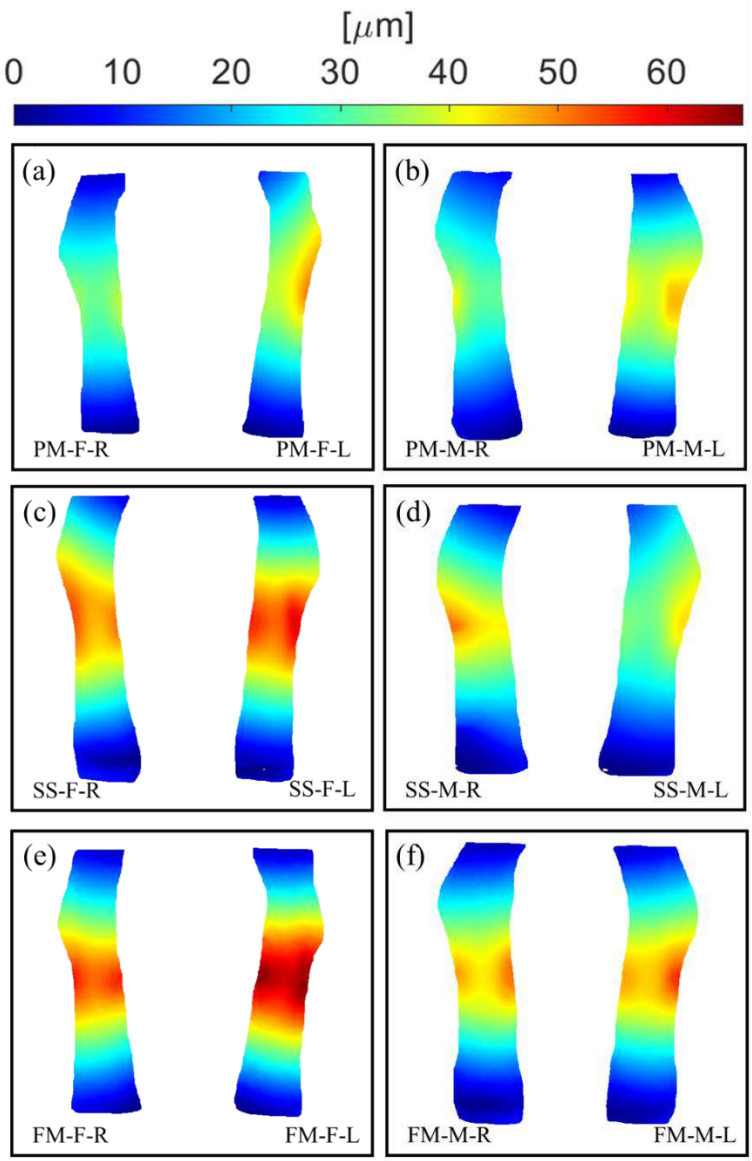

Figure 43. Total surface deformation observed in the femurs just before the fracture for females and males, (a)(b) post mortem, (c)(d) saline solution, and (e)(f) formaldehyde bones.

By retrieving the maximum deformation for each bone and method, a chart is created to determine if the preservation method modifies the mechanical response. The latter is illustrated in Figure 44a, where it is possible to see differences between surface and internal displacements. Furthermore, when considering gender, it becomes clear that female bones can withstand more deformations than their male counterparts before reaching a fracture, as depicted in Figure 44b.

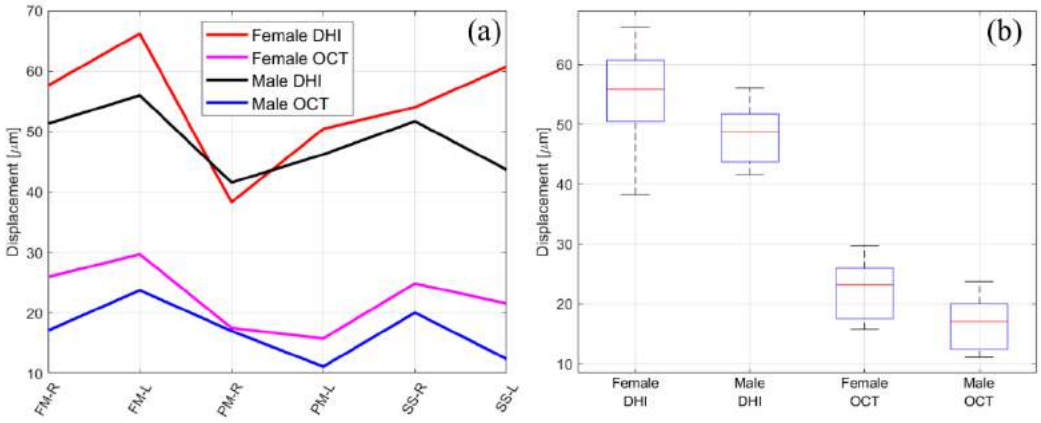

Figure 44. Comparison of (a) maximum displacements and (b) gender results by method.

The internal displacement is mainly observed across the marrow, which is less deformed than the cortical bone in contact with the tip of the SM. The latter results in more extensive deformations at the exterior, while the center helps to contain the femur's deformation. It is also observed that the right and left formaldehyde bones describe nearly parallel lines (see Figure 44a); meanwhile, the rest do not show this uniform behavior. The bone's viscoelasticity is responsible for these changes in the PM and SS bones, but the FM bones lose this condition.

For comparison purposes, all samples were analyzed via Raman spectroscopy. Figure 45a and Figure 45b show the mean Raman spectra from male and female femoral bones, respectively. These spectra are very similar to those reported in previous studies [93,94], where the most intense Raman peaks correspond to the phosphate (ν1) and the strongest C-H vibrational line at 960 cm^{-1} and 2945 cm^{-1}, respectively. The three group signals (FM, SS, and PM) of Figure 45a and Figure 45b show that the spectra do not indicate significant differences in their intensity profile. Figure 45c shows the average spectrum response for each group without gender distinction and looks similar to Figure 45a and Figure 45b. This observation suggests that the bone's mechanical condition might be consistent across all three preservation conditions for single-point analysis but not for a full field inspection such as DHI and FD-OCT.

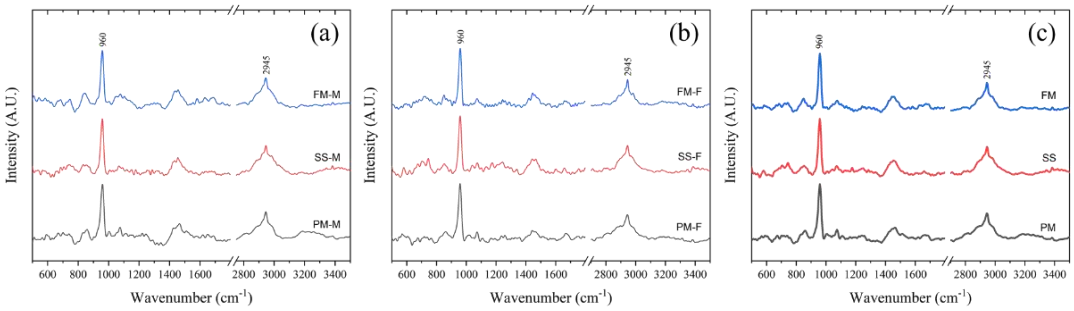

Figure 45. Mean Raman spectra for (a) male, (b) female, and (c) full average. Peaks obtained at 960 cm^{-1} and 2945 cm^{-1} correspond to phosphate v1 and the strongest C-H vibrational line.

4. Conclusions and future work

In this work, two projects based on interferometric techniques were introduced. The first project uses a t-DHI configuration to observe water interactions within a water tunnel, focusing on fluid dynamics. The second project investigates the influence of the storage media on the full-field mechanical response of femoral mice bones, using simultaneously DHI and FD-OCT. DHI and FD-OCT are both non-invasive, full-field interferometric techniques that can be applied to various materials and phenomena. These techniques can retrieve the optical phase difference between two different states of the object under study, which makes them ideal for studying dynamic events. Depending on the experimental setup, DHI can explore transparent media in transmission mode or analyze the surface structure displacements of an opaque material with an out-of-plane configuration. FD-OCT is the ideal option for conducting internal inspections of low-scattered materials.

The results obtained from the observation of the fluid dynamic proved that water under controlled conditions seen with a t-DHI system could render hydrodynamic responses. Also, the optical information can obtain vector fields similar to those from a wind tunnel. Perhaps the main advantage lies in using a smaller tunnel and simple hardware to retrieve the information. The optical phase changes detect the water trajectories without adding markers or density variation agents, highlighting the efficiency and non-invasiveness of the approach.

The system's hydrodynamic response, observed without any object inside the transparent chamber, showed that the water presents a laminar flow behavior once the water is in a constant steady motion. A typical fluid behavior was observed during the barrier test when the water trajectory was forced to deviate. The movement of water surrounding the barrier generates an eddy for the initial interaction with the stagnant water behind the barrier. The liquid flowed freely over the barrier once the static's inertia was broken. The latter proved the capability of the system to capture the water interaction during an entire dynamic test. The car's hydrodynamic response indicates that its hydrodynamic response can be analyzed and compared to its aerodynamic behavior using the displacement retrieved with the optical phase.

The proposed water tunnel employs a minimum of space and resources, which makes it a compact dynamic testing system. Full-field flow visualization with t-DHI is a powerful tool that can provide helpful aerodynamic and hydrodynamic information for an object without external sensors or markers. Two distinct approaches can be pursued to advance this project in the future. The first is to improve the water tunnel system by modifying the water distribution system, representing a significant technical upgrade. Increasing the number of water inlets/outlets beyond the current eight or the distribution and recollection devices can improve fluid stability by adding more flow lines at the entrance, enabling more in-depth studies in hydrodynamics. This enhancement would facilitate a broader range of experiments and more precise analyses of fluid behavior within the system. The second involves transitioning from water to air as the fluid medium for analysis. For this approach, building an air channel system would enable the examination of aerodynamics using t-DHI. This transition offers several advantages, including a cost-effective and compact system suitable for full-field scale measurements. Analyzing aerodynamics in an air channel expands the scope of applications, allowing for comprehensive studies of airflow patterns and dynamics. For further exploration and development, these two approaches promise to expand research

opportunities in fluid dynamics and aerodynamics. In addition, it could lead to applications in diverse fields such as automotive, nautical, aeronautics, and aerospace.

On the other hand, the mechanical test evaluates storage preservation media for hard tissue through mechanical tests conducted on entire mice femoral bones. A difference is observed when comparing the maximum average deformation in female and male bones before fracture. This difference suggests that female bones are more flexible compared to male bones. This flexible characteristic was observed at the bone's surface and inner sections. Larger deformation is observed at the cortical bone (external section), while the internal section is less deformed. Besides the differences between male and female bones, various observations are noted for the different bone groups. The PM group exhibits a viscoelastic and anisotropic behavior during the 3PB deformation due to the interaction of the cortical bone and the inner bone section. It was observed that the SS group keeps its anisotropic response of the bone even after 48 hours of storage, while the FM group with the same immersion time modifies this to an isotropic response.

Additionally, single-point molecular inspection using Raman spectroscopy on these bone groups reveals no difference in their respective spectra. However, full-field tests yield contrasting results. These differences suggest that while the formaldehyde solution alters the bone's full mechanical response, it does not affect its chemical characteristics.

Based on the information gathered, the saline solution could be considered an indicated preservation media for bones under mechanical analyses, even after several hours. This insight is particularly valuable when full-field optical methods are applied to tissue inspection. This information could help store the samples adequately to avoid errors in the mechanical measurements. Formaldehyde preservation leads to physical modifications in the bone marrow, which is observed by agglutination and cluster formation. However, it is also possible to have this result with the saline solution, but less pronounced.

Conducting a Raman spectroscopy analysis of bone tissue preserved in formaldehyde and saline solution is necessary for future work. This analysis will characterize the physical modification induced by each preservation media and provide insights into the tissue's chemical compositions and structural changes. Simultaneously, a mechanical comparison of bones focused on the impact of marrow modifications over the mechanical response will explain how the marrow influences the overall biomechanical response of the bone, providing information on tissue integrity and accuracy in mechanical analyses. These approaches can benefit both research and clinical applications.

References

[1] Gasvik K J, Optical Metrology, 3rd edition (John Wiley & Sons Ldt, West Sussex, England, 2002).

[2] Cuypers W, Van Gestel N, Voet A, Kruth JP, Mingneau J, Bleys P, "Optical measurement techniques for mobile and large-scale dimensional metrology" *Optics and Lasers in Engineering*, 2009; 47: 292-300.

[3] Reid GT, "Automatic fringe pattern analysis: A review", *Optics and Lasers in Engineering*, 1986-1987; 7: 37-68.

[4] Akbari D, and Soltani N, "Investigation of loading parameters in detection of internal cracks of composite material with digital shearography," *World Applied Sciences Journal*, 2013; 21: 526–535.

[5] Tyson J, Schmidt T, and Psilopoulos J, "Optical metrology the key to lean manufacturing," SAMPE Conference, 2015.

[6] Arola A M, Kaijalainen A, Kesti V, Pokka A P, and Larkiola J, "Digital image correlation and optical strain measuring in bendability assessment of ultra-high strength structural steels," *Procedia Manufacturing*, 2019; 29: 398-405. https://doi.org/10.1016/j.promfg.2019.02.154

[7] Vishnoi A, and Rajshekhar G, "Rapid deformation analysis in digital holographic interferometry using graphics processing unit accelerated Wigner–Ville distribution," *Applied Optics*, 2019; 58: 4420 – 4424. https://doi.org/10.1364/AO.58.004420

[8] Gómez-Méndez GA, Martínez-García A, Serrano-García D I, Rayas-Álvarez J A, Pérez AM, Islas-Islas JM, and Toto-Arellano NI, "Measurement in-plane deformations in electronic speckle pattern interferometry using phase-shifting modulated by polarization," *Optics Communications*, 2021; 498: 127245. https://doi.org/10.1016/j.optcom.2021.127245

[9] Fu J, Pierron F, and Ruiz PD, "Elastic stiffness characterization using three-dimensional full-field deformation obtained with optical coherence tomography and digital volume correlation," *Journal of Biomedical Optics*, 2013; 18: 121512. https://doi.org/10.1117/1.JBO.18.12.121512

[10] Osten W and Pedrini G, "55 Years of Holographic Non-Destructive Testing and Experimental Stress Analysis: Is there still Progress to be expected?," *Light: Advanced Manufacturing*, 2022; 3: 121-136. https://doi.org/10.37188/lam.2022.008

[11] Motra HB, Hildebrand J, and Dimmig-Osburg A, "Assessment of strain measurement techniques to characterize mechanical properties of structural steel," *Engineering Science and Technology, an International Journal*, 2014; 17: 260–269. https://doi.org/10.1016/j.jestch.2014.07.006

[12] Bruno L, "Mechanical characterization of composite materials by optical techniques: A review," *Optics and Lasers in Engineering*, 2018; 104: 192-203. https://doi.org/10.1016/j.optlaseng.2017.06.016

[13] Silva Acosta JL, Mendoza Santoyo F, Flores Moreno M, Hernández Montes M d S, De la Torre Ibarra MH, Frausto Rea G, Muñoz S, and Hernández EEL "Study of skin aging effects induced by near UV radiation using time average digital holographic interferometry," *Optics and Lasers in Engineering*, 2021; 137: 106345. https://doi.org/10.1016/j.optlaseng.2020.106345

[14] Kumar M, Shakher C, "Measurement of temperature and temperature distribution in gaseous flames by digital speckle pattern shearing interferometry using holographic optical element," *Optics and Lasers in Engineering,* 2015;73:33-39.

[15] Saucedo T, Mendosa Santoyo F, De La Torre-Ibarra M, Pedrini G, Osten W, "Endoscopic pulsed digital holography for 3D measurements," *Optics Express*, 2006;14:1468-1475.

[16] Briones-R M de J, De La Torre-Ibarra M, Mendoza-Santoyo F, and Pedroza-G. J, "Simultaneous birefringence imaging and depth phase resolved measurement using a Fourier domain OCT system," *Optics and Lasers in Engineering*, 2015; 68: 104-110.
https://doi.org/10.1016/j.optlaseng.2014.12.005

[17] De La Torre MH, Frausto-Reyes C, Moreno D and Salgado-Transito I, "Flame analysis using a simple transmission digital holographic interferometer," *Applied Optics*. 2021;60:5623-5628.

[18] Mehta RD and Bradshaw P, "Design rules for small low speed wind tunnels," *Aeronautical Journal*, 1979; 83:443-449.

[19] Calautit JK, Chaudhry HN, Hughes BR, and Sim LF, "A validated design methodology for a closed-loop subsonic wind tunnel," *Journal of Wind Engineering and Industrial Aerodynamics*, 2014;125:180-194.

[20] Yukun F, Zuogang C, Yi D, Zheng Z, Ping W, "An experimental and numerical investigation on hydrodynamic characteristics of the bow thruster," *Ocean Engineering,* 2020;209:107348.

[21] Evans B, Townsend J, Hassan O, Morgan K, Ayers K, Chapman K, Green A, "On the subsonic and low transonic aerodynamic performance of the land speed record car, Bloodhound LSR," Proceedings of the Institution of Mechanical Engineers, *Part G: Journal of Aerospace Engineering*, 2022;236:1895-1921.

[22] Fei X, Jessing C, Kuthada T, Wiedemann J, Wagner A, "The Influence of Different Unsteady Incident Flow Environments on Drag Measurements in an Open Jet Wind Tunnel," *Fluids*, 2020;5:178.

[23] Sathishkumar M, Nema A, Das Patel K, "Experimental analysis of aerodynamic drag reduction of a hatchback model car by rear spoiler in the wind tunnel," *International Journal of Mechanical and Production Engineering Research and Development,* 2018; 8:991-1000.

[24] Liu M, Xiao L, Yang L, "Experimental investigation of flow characteristics around four square-cylinder arrays at subcritical Reynolds numbers", *International Journal of Naval Architecture and Ocean Engineering*, 2015;7:906-19.

[25] Rolin V, Porté-Agel F, "Wind-tunnel study of the wake behind a vertical axis wind turbine in a boundary layer flow using stereoscopic particle image velocimetry," *J. Phys.: Conf. Ser*., 2015;625:012012.

[26] Zhu G, Feng Y, Chen Z, Lu H, "Hydrodynamic design of a circulating water channel based on a fractional-step multi-objective optimization," *Ocean Engineering,* 2022;251:110959.

[27] Salmon F, Chatellier L, "3D fluid–structure interaction simulation of an hydrofoil at low Reynolds number," *Journal of Fluids and Structures*, 2022;111:103573.

[28] Liu X, Yuan X, Luo K, WangY, "Blockage effect of a wall on the hydrodynamic characteristics of a supercavitating vehicle's aft body," *Ocean Engineering,* 2022;256:111564.

[29] Semeraro FF, Schito P, "Numerical Investigation of the Influence of Tire Deformation and Vehicle Ride Height on the Aerodynamics of Passenger Cars," *Fluids* 2022;7:47.

[30] Ramaiah J, Ajithaprasad S, Gannavarpu R, Ambrosini, D, "Fast and robust method for flow analysis using GPU assisted diffractive optical element based background oriented schlieren (BOS)," *Optics and Lasers in Engineering*, 2020;126:105908.

[31] Poon TC, Digital Holography and three-dimensional display: Principles and Applications, 1st edition (Springer Science and Business Media, 2016).

[32] Awatsuji Y, Parallel phase-Shifting Digital Holography, in *Multi-dimensional Imaging*, 1st edition (John Wiley and Sons Ltd., 2014).

[33] Frausto-Rea G, De La Torre MH, Flores JM, Silva L, Briones RM, Mendoza Santoyo F, "Micrometric size measurement of biological samples using a simple and non-invasive transmission interferometric set up," *Optics Express*, 2019;27:26251-26263.

[34] De La Torre MH, Frausto-Rea G, Mendoza-Santoyo F, Hernandez Montes MS, "I, Fish swim water bulk displacement visualization with digital holographic interferometry," *Applied Optics*, 2021;90:537681.

[35] Frausto-Rea G, De la Torre-Ibarra MH, Muñoz-Huerta RF, and Casillas FJ, "Mechanical test study in composites using digital holographic interferometry and optical coherence tomography simultaneously," *Applied Optics*, 2020;59:857–865. https://doi.org/10.1016/S1350-4533(98)00007-1

[36] Feng X, "Chemical and biochemical basis of cell-bone matrix interaction in health and disease," *Current Chemical Biology*, 2009;3:189 – 196. https://doi.org/10.2174/187231309788166398

[37] Seeman E, "Bone quality: The material and structural basis of bone strength," *Journal of Bone and Mineral Metabolism*, 2008;26:1–8. https://doi.org/10.1007/s00774-007-0793-5

[38] Li S, Demirci E, and Silberschmidt VV, "Variability and anisotropy of mechanical behavior of cortical bone in tension and compression," *Journal of the Mechanical Behavior of Biomedical Materials*, 2013;21:109–120. https://doi.org/10.1016/j.jmbbm.2013.02.021

[39] Zioupos P, Currey JD, Mirza MS, and Barton DC, "Experimentally determined microcracking around a circular hole in a flat plate of bone: comparison with predicted stresses.," Philosophical transactions of the Royal Society of London. Series B, *Biological sciences*, 1995;347:383–396. https://doi.org/10.1098/rstb.1995.0031

[40] Rho JY, Kuhn-Spearing L, and Zioupos P, "Mechanical properties and the hierarchical structure of bone," *Medical Engineering and Physics*, 1998;20:92 – 102. https://doi.org/10.1016/S1350-4533(98)00007-1

[41] Rho Y, Tsui TY, and Pharr GM, "Elastic properties of human cortical and trabecular lamellar bone measured by nanoindentation," *Biomaterials*, 1997;18:1325–1330. https://doi.org/10.1016/S0142-9612(97)00073-2

[42] Tavera Ruiz CG, De La Torre-Ibarra MH, Flores-Moreno JM, Frausto-Reyes C and Mendoza Santoyo F, "Cortical bone quality affectations and their strength impact analysis using holographic interferometry," *Biomedical Optics Express*, 2018;9:4818–4833. https://doi.org/10.1364/BOE.9.004818

[43] Tavera Ruiz CG, De La Torre MH, Flores-Moreno JM, Hernandez MdS, Mendoza-Santoyo F, Briones MdJ, and Sanchez JP, "Surface structural damage study in cortical bone due to medical drilling," *Applied Optics*, 2017;56:179–188. https://doi.org/10.1364/AO.56.00F179

[44] Knox AM, McGuire AC, Natoli RN, Kacena MA, and Collier CD, "Methodology, selection, and integration of fracture healing assessments in mice," *Journal of Orthopedic Research*, 2021;39:2295 –2309. https://doi.org/10.1002/jor.25172

[45] Sánchez Alvarez A, De La Torre Ibarra MH, Mendoza Santoyo F, and Saucedo Anaya T, "Strain determination in bone sections with simultaneous 3D digital holographic interferometry," *Optics and Lasers in Engineering*, 2014;57:101–108. https://doi.org/10.1016/j.optlaseng.2014.01.022

[46] Stefan U, Michael B, and, Werner S, "Effects of three different preservation methods on the mechanical properties of human and bovine cortical bone," *Bone*, 2010;47:1048 – 1053. https://doi.org/10.1016/j.bone.2010.08.012

[47] Zhang G, Deng X, Guan F, Bai Z, Cao L and Mao H, "The effect of storage time in saline solution on the material properties of cortical bone tissue," *Clinical Biomechanics*, 2018;57:56 – 66. https://doi.org/10.1016/j.clinbiomech.2018.06.003

[48] Von Euw S, Wang Y, Laurent G, Drouet C, Babonneau F, Nassif N and Azaïs T, "Bone mineral: new insights into its chemical composition," *Scientific Reports*, 2019;9:8456. http://doi.org/10.1038/s41598-019-44620-6

[49] Menger MM, Manuschewski R, Ehnert S, Rollmann MF, Maisenbacher TC, Tobias AL, Menger MD, Laschke MW and Histing T, "Radiographic, Biomechanical and Histological Characterization of Femoral Fracture Healing in Aged CD-1 Mice," *Bioengineering*, 2023;10:275. https://doi.org/10.3390/bioengineering10020275

[50] Morgan EF, Unnikrisnan GU and Hussein AI, "Bone Mechanical Properties in Healthy and Diseased States," *Annual Review of Biomedical Engineering*, 2018;20:119–143. https://doi.org/10.1146/annurev-bioeng-062117-121139

[51] Scărlătescu DD, Modrea A and Stanciu MD, "Three-point Bend Test to Determine the Mechanical Behavior of the Tubes Used in Water Supply Networks," *Procedia Manufacturing*, 2019;23:179-186. https://doi.org/10.1016/j.promfg.2019.02.200

[52] Fercher AF, Drexler W, Hitzenberger CK and Lasser T, "Optical coherence tomography - Principles and applications," *Reports on Progress in Physics*, 2003;66:239–303. https://doi.org/10.1088/0034-4885/66/2/204

[53] De Boer JF, Leitgeb R, and Wojtkowski M, "Twenty-five years of optical coherence tomography: the paradigm shift in sensitivity and speed provided by Fourier domain OCT [Invited]," *Biomed. Opt. Express*, 2017;8:3248-3280. https://doi.org/10.1364/BOE.8.003248

[54] Stritzel J, Rahlves M, and Roth B, "Refractive-index measurement and inverse correction using optical coherence tomography," *Opt. Lett*., 2015;40:5558-5561. https://doi.org/10.1364/OL.40.005558

[55] Pedrini G and Osten W, "Time resolved digital holographic interferometry for investigations of dynamical events in mechanical components and biological tissues," *Strain*, 2007;43:240-249. https://doi.org/10.1111/j.1475-1305.2007.00341.x

[56] Martinez-Garcia V, Wenzelburguer M, Killinger A, Pedrini G, Gadow R, and Osten W, "Residual stress measurement with laser-optical and mechanical methods," *Adv. Mater. Res*., 2014;996:256-261. 10.4028/www.scientific.net/AMR.996.256

[57] De la Torre MH, Flores JM, Aguayo DD, Hernández-Montes MS, Pérez-López C, and Mendoza-Santoyo F, "Displacement measurements over a square meter area using holographic interferometry," *Optical Engineering*, 2014;59:092009. https://doi.org/10.1117/1.OE.53.9.092009

[58] Scărlătescu DD, Modrea A and Stanciu MD, "Three-point Bend Test to Determine the Mechanical Behavior of the Tubes Used in Water Supply Networks," *Procedia Manufacturing*, 2019;23:179-186. https://doi.org/10.1016/j.promfg.2019.02.200

[59] Gabor D, "A new microscope principle," *Nature*, 1948;161:777-778.

[60] Hariharan P, Basics of holography. (New York, Cambridge University Press, 2002).

[61] Kreis T, Handbook of Holographic Interferometry, Optical and Digital Methods. (Wheinheim, WILEY-VCH GmbH & Co. KGaA, 2005).

[62] Takeda M, Ina H, and Kobayashi S, "Fourier-transform method of fringe-pattern analysis for computer-based topography and interferometry," *J. Opt. Soc. Am*., 1982;72(1):156.

[63] De La Torre MH, Hernández Montes MS, Flores-Moreno JM, Mendoza Santoyo F. "Laser speckle based digital optical methods in structural mechanics: a review," *Optics and Lasers in Engineering*, 2016;87:32-58.

[64] De La Torre Ibarra MH, Mendoza Santoyo F, and Hernández-M. MS, "Transmission out-of-plane interferometer to study thermal distribution in liquid," *Optics Letters*, 2018; 43, 871-874.

[65] Boudux C, Fundamentals of Biomedical Optics (Pollux editions, Montréa,2016).

[66]. F. Mendoza-Santoyo, M.H. De la Torre-Ibarra, M. S. Hernández-Montes, J.M. Flores, Optical coherence tomography, in *Full field optical metrology and Applications*, (IOP Publishing, Bristol, UK, 2022). https://doi.org/10.1088/978-0-7503-3027-5

[67] De La Torre-Ibarra MH, Ruiz PD, and Huntley JM, "Double-shot depth-resolved displacement field measurement using phase-contrast spectral optical coherence tomography." *Optics express* 2006;14(21):9643-9656.

[68] Huntley JM, "Automated Analysis of Speckle Interferograms," in Proceedings of Digital Speckle Pattern Interferometry and Related Techniques, P. K. Rastogi ed., (Chichester, West Sussex, England, John Wiley & Sons., 2001) pp. 59-139.

[69] Batchelor GK, An Introduction to Fluid Dynamics (United Kingdom, Cambridge University Press, 2000).

[70] Currie IG, Fundamental Mechanics of Fluids, 4th ed. (Boca Raton, CRC Press, 2013).

[71] Currey JD, Skeletal biomineralization: patterns, process and evolutionary trends (American Geophifical Union, 1983).

[72] Mueller KH, Trias A, Ray RB, "Bone density and composition. Age-related and pathological changes in water and mineral content," *J Bopne Joint Surg Am*, 1966;48:140-148.

[73] Meyers MA, Po-Yu Chen, "Biological materials: Structure and mechanical properties," *Progress in Materials Science* 2008;53:1‑206.

[74] Weiner S, Traub W, "Bone structure: from angstroms to microns," *FASEB* 1992;6:879–885.

[75] Rho JY., Kuhn-Spearing L., Zioupus P., "Mechanical properties and the hierarchical structure of bone," *Medical Engineering & Physics*, (1998); 20, 92-108.

[76] Carter DR, Hayes W, "The compressive behavior of bone as a two-phase porous structure," *J Bone Jt Surg*, 1977;59A:954–962.

[77] Giraud-Guille MM, "Twisted plywood architecture of collagen fibrils in human compact bone osteons," *Calcif Tissue Int*, 1988;42:167–80.

[78] Glimcher M J, "Mechanism of Calcification: Role of collagen fibrils and collagen-phosphoprotein complexes in vitro and in vivo," *The Anatomical Record*, 1989; 224:139-153.

[79] Knudson D., Fundamentals of Biomechanics, 2nd Edition, (Springer California State University at Chico, 2007).

[80] Morgan E F, Unnikrisnan GU, and Hussein A I, "Bone mechanical properties in healthy and diseased states," *Annu Rev Biomen Eng*, 2018; 20, 119-143. doi:10.1146/annurev-bioeng-062117-121139

[81] Zioupos P, Hansen U, Currey JD "Microcracking damage and the fracture process in relation to strain rate in human cortical bone tensile failure," *J Biomech*. 2008; 41:2932–2939.

[82] Hall SJ. Basic biomechanics. 4th ed. (Boston: McGraw-Hill; 2003).

[83] Broniszewski J, Piechna JR, "Fluid-Structure Interaction Analysis of a Competitive Car during Brake-in-Turn Manoeuvre," *Energies* 2022;15.

[84] Cai J, Kapoor S, Sikder T, He Y. "Effects of Active Aerodynamic Wings on Handling Performance of High-Speed Vehicles," SAE Technical Papers 2017.

[85] Zakher BN, Elhadary M, El-Gohary MA, El Fahham IM, "Comparison Between Experimental Life Road Simulation and Computational Fluid Dynamics and Fluid Structure Interaction for Sedan Car," *CFD Letters* 2022;14:81-97.

[86] Stefan U, Michael B and Werner S, "Effects of three different preservation methods on the mechanical properties of human and bovine cortical bone," *Bone*, 2010;47:1048 – 1053. https://doi.org/10.1016/j.bone.2010.08.012

[87] Zhang G, Deng X, Guan F, Bai Z, Cao L and Mao H, "The effect of storage time in saline solution on the material properties of cortical bone tissue," *Clinical Biomechanics*, 2018;57:56 – 66. https://doi.org/10.1016/j.clinbiomech.2018.06.003

[88] "Ethical Guidelines for the Use of Animals in Research," Published on 08/07/2019. https://www.forskningsetikk.no/en/guidelines/science-and-technology/ethical-guidelines-for-the-use-of-animals-in-research/

[89] Azzam A, and Li W, "An experimental investigation on the three-point bending behavior of composite laminate," Global Conference on Polymer and Composite Materials, Ningbo, China, 27–29 May 2014. https://doi.org/10.1088/1757-899X/62/1/012016

[90] Deckard C, Walker A and Hill BJF, "Using three-point bending to evaluate tibia bone strength in ovariectomized young mice," *Journal of Biological Physics*, 2017;43:139 – 148. 10.1007/s10867-016-9439-y

[91] Orlando A, Franceschini F, Muscas C, Pidkova S, Bartoli M, Rovere M, and Tagliaferro A, "A comprehensive review on Raman Spectroscopy applications," *Chemosensors*, 2021;9:262. https://doi.org/10.3390/chemosensors9090262

[92] Berrones-Guerrero JD, Frausto-Reyes C, De la Torre MH, Ortiz-Morales M, and Lopez-T. JM, "Impacto n the Raman spectra of liquids when a polarized light source is used," *Spectrochim Acta A Mol Biomol Spectrosc*, 2022;272:121001. 10.1016/j.saa.2022.121001

[93] Bi X, Patil CA, Lynch CC, Pharr CM, Mahadevan-Jansen A and Nyman JS, "Raman and mechanical properties correlate at whole bone- and tissue-levels in a genetic mouse model," *Journal of Biomechanics*, 2011;44:297 – 303.

[94] Leikin S, Parsegian VA, Yang WH, and Walrafen GE, "Raman spectral evidence for hydratation forces between collagen triple helices," *Proc. Natl. Acad. Sci. USA*, 1997;94:11312 – 11317. https://doi.org/10.1073/pnas.94.21.11312

Appendix A

The hardware development of the water tunnel system

The initial schematic design of the water system is illustrated in Figure A1. Due to the direct correlation between the velocity within the transparent chamber and the water inlet velocity was decided to initiate the chamber's design. After that, several inlet configurations were tested for a controlled flow through the chamber.

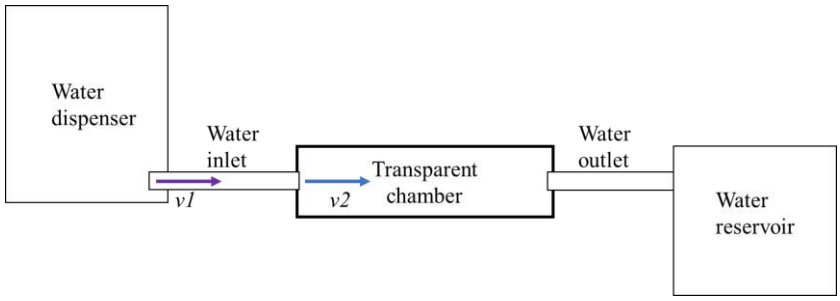

Figure A1. Initial schematic design.

The layout of the transparent chamber is shown in Figure A2. It consists of a transparent layer of PMMA (Poly-methyl-methacrylate) 6mm thick panels, with 500 x 50 x 100 mm in length, width, and height, respectively. These dimensions were selected for two reasons:

1) The collimated beam of the optical setup had a 25 cm diameter, allowing it to illuminate more than 1/3 of this chamber's length.
2) The water inside the chamber weighs > 5 kg; a bigger chamber will complicate its mobility during this proof of principle.

The side covers around the open sections connect the chamber with the water inlet and outlet.

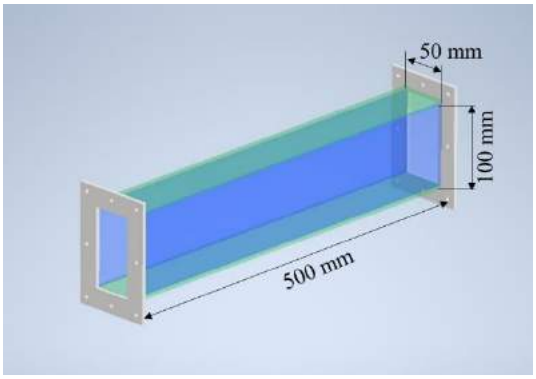

Figure A2. Transparent chamber digital design.

A first configuration (figure A3), with the water distribution (inlet) of one CPVC tube of ¾" in diameter, is prepared. The water outlet (recollection) has a similar design. Both structures are connected to the chamber with rectangular clamps at both ends. Colorants were used to observe the water interaction within the transparent chamber. Figure A4 shows a sequence of images when water enters the chamber after the valve opens. Please be aware that the chamber has already filled with clear water, and the colored water starts moving once the valve opens. At the entrance, the water moves faster in the central region than on the chamber's edges. The obtained flow in this configuration is non-linear; the observed flow has a turbulent response at the entrance.

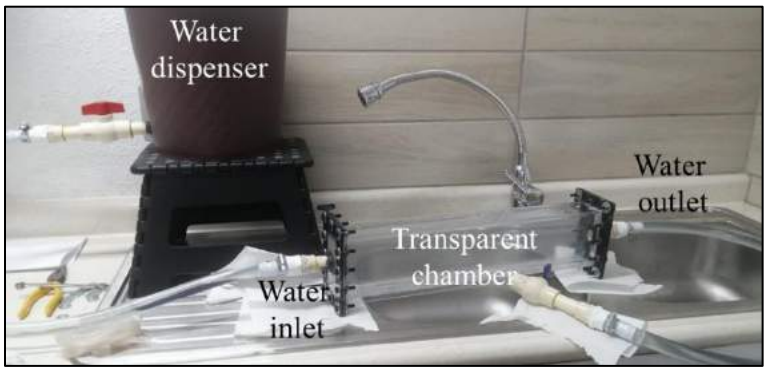

Figure A3. First configuration.

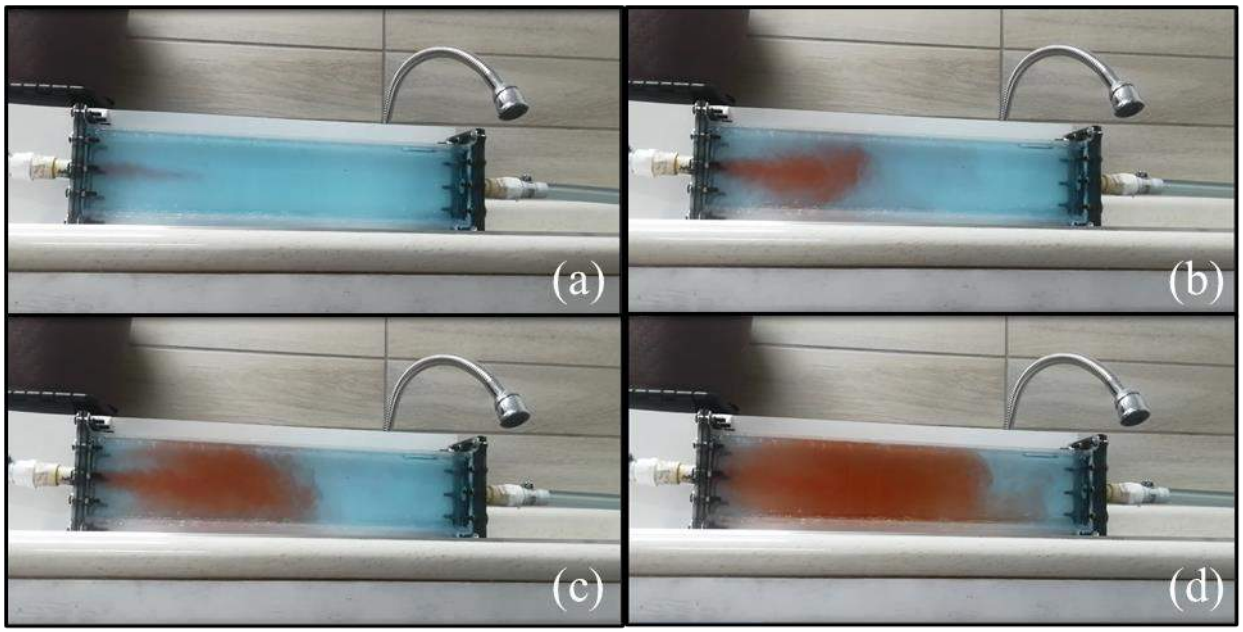

Figure A4. Water flow observed with the first configuration at different times: (a) t1, (b) t2, (c) t3, and (d) t4.

In order to improve the flow response, a second configuration is proposed. Here, the optimization of the water inlet and outlet (called water distribution (WD) and recollection (WR) devices) is the target. In contrast to the first version, which uses a ¾" tube, this second version incorporates eight tubes of ½" diameter distributed over the cross-section area of the chamber, as shown in Figure A5a. Figure A5b shows this water tunnel configuration, where the water flow is directed through transparent hoses using the water distributor (WD).

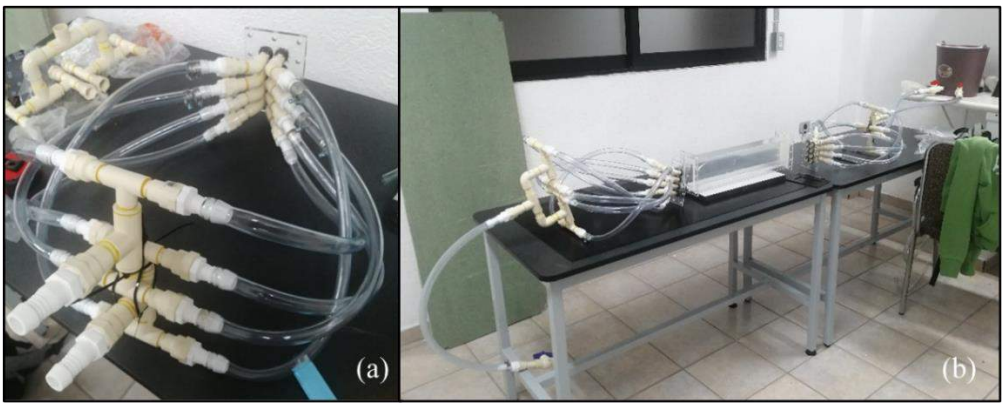

Figure A5. View of the (a) WD and (b) second water tunnel configuration.

Figure A6 depicts a sequence of the flow patterns inside the chamber. It is observed that the flow distribution using the flexible hoses is not uniform; however, a controlled flow was noted as the water entered the chamber (highlighted in the blue circle in Figure A6b). According to this result, it was decided to keep the 8-inlet distribution but to modify the water distribution.

Figure A6. Water flow obtained with the second configuration.

The third version keeps the 8-inlet configuration but replaces the hoses for CPVC tubes, as observed in Figure A7a. Figure A7b displays an image of the entire water distributor (WD) device using two main injection routes. These modifications resulted in a uniformly distributed water flow at the chamber's entrance, as shown in Figure A8. A slightly higher flow rate in the lower zone of the chamber was observed, and it is associated with gravity. However, a distinct area of uniform distribution (highlighted with a blue circle) was identified. This region was selected to conduct flow interaction tests.

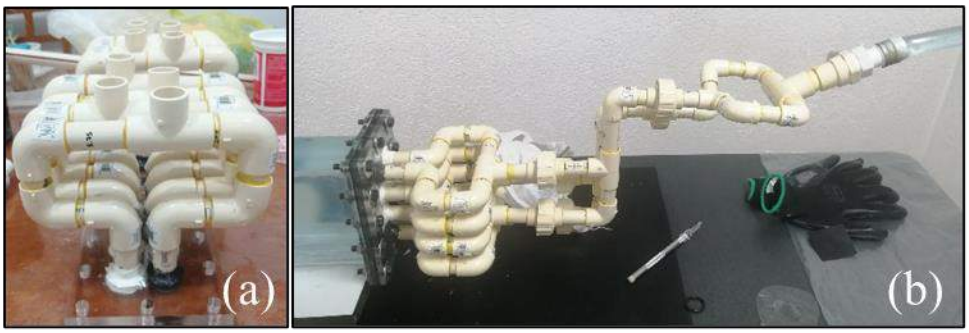

Figure A7. (a) The 8-inlet system uses CPVC tubes to direct the flow and (b) the water distribution device of the third water tunnel configuration.

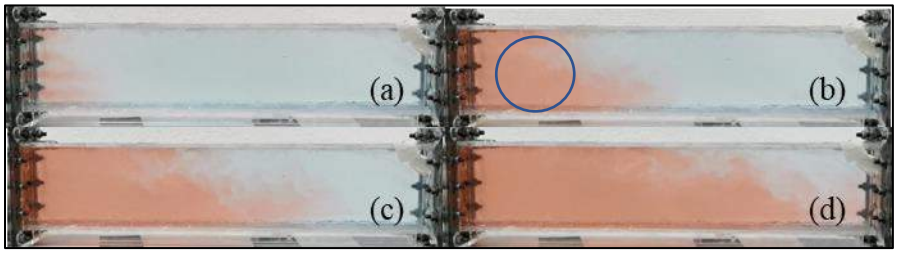

Figure A8. Water flow obtained with the third configuration.

The fourth and final version of the water tunnel system was derived from the latter configuration by incorporating additional flow control devices. These include a submersible water pump to maintain the water circulating and a plastic grid block positioned at the beginning of the chamber that keeps the direction of the flow lines longer. Several control valves are added to regulate the water velocity, enhancing the overall efficiency and control of the water flow. Figure A9 shows a sequence of the water flow inside the transparent chamber of the water tunnel system. Here, the four levels of flow injection can be observed (Figure A9a). Furthermore, the flow primarily covers the cross-section of the chamber, as observed in Figure A9b. Although gravity causes the flow rate to be higher at the bottom of the chamber, no eddies are observed, indicating a constant flow (Figure A9c and A9d).

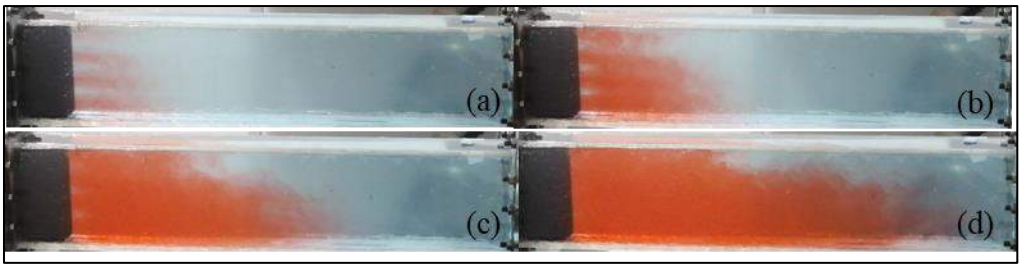

Figure A9. Water flow obtained with the final water tunnel configuration.

Once a constant flow is observed, it is possible to proceed with the optical tests using the t-DHI configuration where any colorant is used.